(2)

AD-A270 125

PL-TR-93-2102(II)

ANALYSIS OF REGIONAL BODYWAVE PHASES FROM EARTHQUAKES IN WESTERN CHINA

Jeffrey S. Barker

Department of Geological Sciences
State University of New York
Binghamton, NY 13902-6000

June 17, 1993

Final Report (Part II)
1 August 1991 - 1 February 1993

APPROVED FOR PUBLIC RELEASE, DISTRIBUTION UNLIMITED.

PHILLIPS LABORATORY
Directorate of Geophysics
AIR FORCE MATERIEL COMMAND
HANSCOM AIR FORCE BASE, MA 01731-3010

This technical report has been reviewed and is approved for publication.

JAMES F. LEWKOWICZ
Contract Manager
Solid Earth Geophysics Branch
Earth Sciences Division

JAMES F. LEWKOWICZ
Branch Chief
Solid Earth Geophysics Branch
Earth Sciences Division

DONALD H. ECKHARDT, Director
Earth Sciences Division

REPORT DOCUMENTATION PAGE

Form Approved
OMB No 0704-0188

1. AGENCY USE ONLY *(Leave blank)*

2. REPORT DATE
17 June 1993

3. REPORT TYPE AND DATES COVERED
Final (1 Aug 1991-1 Feb 1993) Volume II

4. TITLE AND SUBTITLE
Analysis of Regional Bodywave Phases from Earthquakes in Western China

5. FUNDING NUMBERS
PE 62101F
PR 7600 TA 09 WU AR

Contract F19628-90-K-0042

6. AUTHOR(S)
Jeffrey S. Barker

7. PERFORMING ORGANIZATION NAME(S) AND ADDRESS(ES)
State University of New York
Department of Geological Sciences
Binghamton, NY 13902-6000

8. PERFORMING ORGANIZATION REPORT NUMBER

9. SPONSORING/MONITORING AGENCY NAME(S) AND ADDRESS(ES)
Phillips Laboratory
29 Randolph Road
Hanscom AFB, MA 01731-3010

Contract Manager: James Lewkowicz/GPEH

10. SPONSORING/MONITORING AGENCY REPORT NUMBER
PL-TR-93-2102 (II)

11. SUPPLEMENTARY NOTES

12a. DISTRIBUTION/AVAILABILITY STATEMENT
Approved for public release;
distribution unlimited

12b. DISTRIBUTION CODE

13. ABSTRACT *(Maximum 200 words)*

Broad-band regional body-wave data have been collected and modeled for three profiles of earthquakes recorded at CDSN station WMQ in western China. The first profile is from earthquakes located to the southwest, within the Tienshan and Tarim basin. The second is from earthquakes to the NNE across the Altai mountains and the western tip of Mongolia and into Siberia. The third profile is from earthquakes to the SSE, some near the Lop Nor test site, and others from the Altyn Tagh and Qaidam Basin. Plane-layered velocity structure models were determined for each profile, and synthetic seismograms were computed using a frequency-wavenumber integration technique. For each earthquake, an appropriate source mechanism is assumed, and synthetic seismograms are computed for source depths of 10, 20 and 30 km. The modeling demonstrates that regional P_n-P_{pg} wavetrains result from the interference of several phases. Since some of these depart the source upward and others depart downward, this interference is sensitive to source depth and source mechanism. Therefore, as long as accurate synthetic seismograms can be computed, modeling these phases can serve as a powerful discriminant of earthquakes and explosions.

14. SUBJECT TERMS
Broadband regional seismograms, Crustal phases, Bodywaves, Crustal phases, China, Discriminants

15. NUMBER OF PAGES
54

16. PRICE CODE

17. SECURITY CLASSIFICATION OF REPORT	18. SECURITY CLASSIFICATION OF THIS PAGE	19. SECURITY CLASSIFICATION OF ABSTRACT	20. LIMITATION OF ABSTRACT
Unclassified	Unclassified	Unclassified	SAR

NSN 7540-01-280-5500

Standard Form 298 (Rev 2-89)
Prescribed by ANSI Std Z39-18
298-102

TABLE OF CONTENTS

LIST OF FIGURES

LIST OF TABLES

ANALYSIS OF REGIONAL BODYWAVE PHASES FROM EARTHQUAKES IN WESTERN CHINA

OBJECTIVE:

The purpose of this study is to improve our understanding of the regional crustal waveguide phases encompassed by P_n and P_g (often termed P_{nl}), by modeling regional waveforms in eastern Asia. Saikia and Burdick (1991) showed that deterministic modeling of short-period P_{nl} can provide a good fit to waveforms at ranges of 200 to 420 km from NTS explosions. Zhao and Helmberger (1991) have demonstrated similar success in modeling broad-band P_{nl} from the Saguenay earthquake recorded at HRV, while Burdick et al. (1992) modeled regional earthquake recordings at the IRIS station, Garm.

If we want to understand the development and propagation of P_{nl}, we must have observations at a number of ranges from the source. Unfortunately, while high-quality, broad-band seismometers are now available in China and the former Soviet Union, the station spacing is quite sparse. In a previous report, we presented the results of modeling a profile of earthquakes recorded at the Chinese Digital Seismic Station, WMQ (Barker, 1991; Wu and Barker, 1992). Since the earthquakes have different depths, magnitudes and mechanisms, this is not the reciprocal problem to wave propagation from a single source to a number of stations. However, by modeling simultaneously waveforms from each of these earthquakes, we gain an understanding not only of the propagation of specific crustal phases near WMQ, but also of the kinds of variation observed for different source depths and mechanisms.

Since the conclusions reached in modeling waveforms from a single profile of earthquakes are radiation-pattern dependent, we now present the results of similar waveform modeling studies, but using profiles of earthquakes along three different azimuths from WMQ (Figure 1; Table 1). The first is a repeat of the previous study of earthquakes southwest of WMQ. These events occurred within the crust in the Tienshan region, and propagated along the structural trend of the Tienshan and the Tarim Basin. A second profile is located to the NNE of WMQ, through the western tip of Mongolia and into Siberia. The third profile is SSE of WMQ, including earthquakes in the vicinity of the Lop Nor Test Site. The propagation paths cross the eastern margin of the Tienshan, the Tarim Basin and, at the largest distances, the Altyn Tagh and Qaidam Basin.

RESEARCH ACCOMPLISHED:

SW Profile

As a first profile, we consider earthquakes along a line SW of WMQ (Figure 1 and Table 1), from the Tarim Basin and the Tienshan regions of western China. In a surface wave regionalization study (Wu and Jones, "Surface wave regionalization and tomography in China and its vicinity", in Wu and Barker, 1992), these are considered to be within the same structural region, so lateral variations in crustal structure should be minimal. These are shallow crustal earthquakes (depths 8-33 km) with thrust mechanisms. Broad-band seismograms have been processed to facilitate comparison with synthetic seismograms. This processing includes time integration (to ground displacement) and a high-pass Butterworth filter (frequency 0.08 Hz) to reduce low-frequency drift in the synthetics. In this study we are concentrating on the P_n-P_g wavetrain, so only the vertical component is modeled.

A profile of the vertical-component waveforms is shown on the left side of Figure 2. Superimposed on the waveforms are travel-time curves appropriate for various P and S phases for a source at 30 km depth in a layered velocity structure model (discussed below). To facilitate comparison between events, the waveforms in this figure and the next have been band-pass filtered from 0.5 - 2.0 Hz, similar to the WWSSN short-period band. Also time shifts have been applied to three of the records: for events 87005 (560 km) and 87159 (1175 km), a time lead of 2 sec is used, while for event 87351 (422 km) a lag of 3 sec is used. These may reflect errors in the assumed origin time of these events, or simply variations due to source depth. The first 50 sec of these waveforms, which includes the P_n-P_g wavetrain, are shown on the left side of Figure 3, along with travel-time curves for selected phases. A number of features in the observed waveforms correlate with some of these predicted arrivals. In particular, for the closest event, P, pP and S may be identified. Beyond 400 km, P_n and P may be identified, but the Moho reflection, P_MP, is not a substantial arrival. In fact, for these mechanisms, sP_n and sP_MP may be seen as an elongated series of arrivals at 400-600 km and as distinct phases at 1175 km. Many other arrivals are present in the observed waveforms; the travel-time curves show only selected arrivals for a single source depth.

Other features are better modeled by computing synthetic seismograms for the appropriate range, depth and mechanism and comparing this with the observed waveform. The velocity structure model assumed (Table 3, Figure 4) is based on the surface wave results of Feng and Teng (1983), modified so that the travel-time curves provide reasonable agreement to observed arrival times (as in Figure 3). The Moho is at a depth of 56 km, while a mid-crustal discontinuity is located at 41 km depth. In the figures to follow, reflections from the Moho are denoted P_MP, while those from the mid-crustal discontinuity are denoted P_CP. A velocity gradient is included in the mantle so that P_n is modeled as a turning ray rather than as a head wave. Synthetic seismograms were computed using a frequency-wavenumber (F-K) integration technique (Barker, 1984). This method uses the compound matrix modification of the Haskell layer matrix method with Filon quadrature over wavenumber. Anelastic attenuation is included to move the poles off of the real-*k* axis. No wavenumber filtering is imposed, so the synthetics include S waves and surface waves in addition to the P wavetrain. These are computation-intensive synthetics, so we must limit the frequency band and time duration (up to 4 Hz, 512 sec duration). The source parameters used in generating the synthetics are listed in Table 2. These include Harvard CMT mechanisms (published in the PDE) when available; otherwise an average mechanism is assumed. Source corner frequencies and Butterworth filter parameters are chosen to give the best agreement between data and synthetics. Source depths (again from the PDE) are sometimes questionable, so the synthetics are computed at 10, 20 and 30 km depths, and the depth closest to that reported for an event is used in the comparison. Generalized ray theory synthetics (Helmberger and Harkrider, 1978) were used to identify specific rays.

Profiles of F-K synthetics for a source depth of 30 km are shown on the right sides of Figures 2 and 3. Although some wrap-around is apparent at the beginning of the traces, P_n and several later arrivals may be easily identified. The synthetics are somewhat simpler than the observed waveforms (compare the two sides of Figure 3), but many features are common. For example, at 400 km sP_n and sP_MP interfere to generate an elongated wavetrain near 20 sec reduced time. Although not shown in the travel-time curves, the second and third P-wave reverberations in the crust also arrive between 20-30 sec (reduced time) at this range. With increasing range, sP_n becomes the dominant phase, interfering with P_MP at 1175 km range. Higher-order crustal multiples (P_MPP_MP, S_MPP_MP, etc.) do not appear to play a dominant role in either the observed or synthetic waveforms for these earthquakes. Certainly the strength of the upgoing S wave that reflects from the free surface is dependent on the radiation pattern, and in this profile we are considering only earthquakes along a single azimuth and with comparable mechanisms. For near-surface isotropic sources (explosions), we would expect crustal multiples to dominate the waveform as Burdick et al. (1989) found for NTS. This is an example of how radiation pattern can cause substantial difference in the generation of the high-frequency P_n-P_g waveform, and may be exploited as a discriminant.

Since the P_n-P_g waveforms result from the interference of a number of phases which depart the source either upward or downward, it is instructive to see how this interference varies with changes in source depth. Shown in Figures 5 - 9 are observed vertical-component waveforms for five of the events in the SW profile, along with F-K synthetics computed for 10, 20 and 30 km source depths. With the exception of event 87279 (Figure 5), the traces have been aligned on the P_n arrival (87279 is at pre-citical range, so is aligned on P). Upward departing phases (such as sP_n) move out in time with increasing source depth, while downward departing phases (such as P_MP) remain stationary or move in. The arrival times of important phases, determined from generalized ray synthetics, are suggested by the lines on the figures. Of course, since we have assumed a layered structure, the change of arrival time with depth is not really linear; the lines are used to help the reader visually interpolate arrivals between the depths we have chosen for computation. Clearly, for different depths and different ranges, different phases interfere to form the arrivals observed on the vertical-component seismograms. For example, for event 87279 (82 km, Figure 5), P_MP is a relatively minor phase, but pP_MP and $(P_CP)_2$ (a double reverberation in the upper crust) interfere at 30 km depth to produce a single large-amplitude arrival, which corresponds to the largest arrival in the observed seismogram. The published depth for this event is 32 km, which is consistent with the depth inferred from the synthetics (slightly deeper than the 30 km synthetics, denoted by the arrow in Figure 5).

For event 87351 (422 km, Figure 6), crustal phases are well separated in time, resulting in the elongated series of arrivals observed for this event. If the depth is somewhat greater than 30 km (as indicated), arrivals observed at about 18 sec and 33 sec may be interpreted as sP_n and $s(P_MP)_2$, respectively. The large-amplitude, late arrival in the synthetics is Sn which, as usual, is substantially larger in the synthetics than in the observed waveform. At 560 km (event 87005, Figure 7), none of the computed synthetics matches the arrival times of all of the observed phases, but from the relative moveout of P_n, P and sP_n, we can see that a source depth of 14-15 km would produce an excellent fit. At this depth, the large arrival at 30 sec results from sP_CP and $s(P_n)_2$. The published depth for this event is 17 km. On the other hand, for event 98024a (731 km, Figure 8), a source depth of about 16 km would provide a better fit (particularly for sP_CP and $s(P_MP)_2$) than the published depth of 30 km. Finally, for event 87159 (1175 km, Figure 9), the published mechanism is clearly inconsistent with the observed P-wave polarities at WMQ. However, since the crustal phases are well separated in time at this range, we interpret that the source must have been shallower than the published depth of 10 km.

NNE Profile

Another profile of earthquakes is located to the NNE of WMQ, crossing the Altai Mountains, through the western tip of Mongolia and into Siberia (Figure 1; Table 1). In this region, very little has been published on the crustal structure. Surface-wave tomography (Wu, 1993) suggests that crustal structure varies slowly along this profile. Therefore, we have developed a crustal velocity structure based on fitting travel-time curves to observed seismograms. Once again, vertical-component broad-band seismograms were obtained from CSS, integrated to ground displacement, and high-pass filtered at 0.08 Hz. The seismograms recorded at WMQ from the NNE profile of earthquakes are shown on the left side of Figure 10, along with travel-time curves computed for a source at 20 km depth in the velocity structure in Table 2. The P_n-P_g portions of these seismograms are plotted on the left side of Figure 11. The linear moveout of P_g (Figure 11) suggests a very low velocity gradient in the crust. P_n goes from 8.15 km/s at 400-600 km range to 8.26 km/s at greater ranges, constraining the mantle gradient. If we identify several observed secondary arrivals with P_MP, the velocity at the base of the crust is 7.4 km/s. Since the depths of some of the earthquakes in this profile are uncertain, and we have little independent constraint on crustal structure, if the source depth is other than 20 km we need to vary the crustal thickness in order to preserve the time separation between P_n and P_g. The resulting velocity structure models are plotted in Figure 12. For sources at 10 km depth, the crustal thickness is 52 km, with a slight gradient at the base of the crust. For 20 km depth, the crustal thickness is 59 km, while for 30 km depth we assume a crustal thickness of 62 km.

Synthetic seismograms were once again computed by the frequency-wavenumber integration technique, for the source parameters listed in Table 3. In this case, the mechanisms are predominantly strike slip, and we assume an increasing normal-fault component to the northeast (toward Lake Baikal). The earthquakes are small enough that the source corner frequency has no effect within the band computed, so the synthetics are simply the impulse response computed to 4 Hz. Butterworth low-pass filters (3.0 Hz) are applied to both observed and synthetic data. The profiles of synthetic seismograms for a source at 20 km depth are plotted on the right sides of Figures 10 and 11. For these profiles, the observed and synthetic seismograms have been bandpass filtered (0.5 - 2.0 Hz) to approximate the WWSSN short-period response. Once again, although the synthetics are simpler than the observed seismograms, the timing and character of P_n, P_g and S_g are quite adequately modeled (Figure 10). Surface reflected phases provide arrivals between P_n and P_g (Figure 11).

The comparisons between seismograms observed at WMQ for each event and synthetics computed for depths of 10, 20 and 30 km are shown in Figures 13-17. The closest event, 87279 (82 km, Figure 13), is the same event included at the closest range in the SW profile. In this case, however, the observed and synthetic seismograms have different filters, and the synthetics are computed for a different mechanism and different structure model. For this mechanism, the largest arrival at about 16 sec is likely the S wave. The next largest arrival (at 20 sec) is pP_MP, suggesting that the source depth is, once again, about 32 km (denoted by the arrow).

Event 87261 is at a range of 388 km and event 88092 is at a range of 439 km. Rather than model each separately, we compare each with synthetics computed for a range of 400 km. For event 87261 (Figure 14), the first arrival is P_n, P_MP is small, and the large arrivals at about 15 sec begin with P_CP and P and are followed by a series of crustal multiples. The best agreement between observed and synthetic waveforms is found between 20 and 30 km depth. Comparing the same synthetics with the observed waveform for event 88092 (Figure 15), we see that P, P_MP and P_CP are very emergent, P arrives somewhat earlier than for event 87261, and the train of crustal multiples is slightly more compact in time. For these reasons, we interpret the depth as 11 km, which is consistent with the depth of 10 km listed in the PDE.

The observed waveform for event 88205 (586 km, Figure 16) is rather noisy and oscillatory. The arrivals in the synthetic seismograms are much more distinct. Nevertheless, we can interpret the large arrival at about 22 sec as the direct P wave, the smaller arrival preceding it as P_CP, and the small first arrival as P_n. With some imagination, P_MP may be identified and, possibly, pP_MP. The large arrivals following the direct P wave are most compact for a shallow source, and become elongated for a deeper source. These pieces of evidence suggest that the source of this event is at about 19 km depth, which is the depth listed in the PDE. The Pn portion of the observed waveform for event 88182 (759 km, Figure 17) is also quite noisy, and prevents an alignment of the waveforms on P_n; therefore we have aligned the synthetics on the P wave. pP_MP precedes the P wave, and can be seen at about 30 sec. Following P are the crustal multiples. From the arrival times of pP_MP, P and $p(P_MP)_2$, we interpret the depth as 16 km. The PDE depth was listed as the default value of 33 km.

SSE Profile

A final profile of earthquakes recorded at WMQ consists of events located to the SSE (Figure 1; Table 1). The closest event (87279) is the same one included in the two previous profiles. Three events are located within the Tarim Basin in the vicinity of the Lop Nor Test Site. Two more distant events are located within the Altyn Tagh and the Qaidam Basin. Propagation from each of these events crosses the Tarim Basin and the eastern margin of the Tienshan before arriving at WMQ. Vertical-component broad-band seismograms were obtained from CSS, integrated to displacement, and low-pass filtered (0.08 Hz). For the profiles, observed and synthetic seismograms have, once again, been band-pass filtered (0.5 - 2.0 Hz). The seismograms recorded at WMQ from the SSE profile of earthquakes are shown on the left side of Figure 18, along with travel-time curves computed for a source at 20 km depth in the velocity structure in Table 2. The P_n-P_g portions of these seismograms are plotted on the left side of Figure 19.

The velocity structure (Figure 20, Table 2) is modified from models of surface wave dispersion in the Tarim Basin and seismic refraction in the Qaidam Basin (SSB, 1986), removing thin low- and high-velocity layers and adjusting crustal thickness and velocities so that the travel-time curves are in agreement with the observed arrival times. As noted in Table 1, there is substantial uncertainty in the depths of the earthquakes listed in the PDE, but those that are well determined fall in the 21-32 km depth range. The travel-time curves are plotted assuming that most of the earthquakes occurred near 20 km depth. If the average depth of the sources is actually deeper, then once again to maintain the time separation between P_n and P_g, the crustal thickness of the model would have to be increased. In our model, crustal thickness is 48 km, which is consistent with estimates based on gravity data (Hu et al., 1989; Shi et al., 1989). For this study, we also assume a plane-layered velocity structure, which would certainly be invalid if we were to consider propagation from earthquakes farther south on the Tibetan Plateau. Surface-wave tomography (Wu, 1993) suggests that crustal thickness varies only slightly in the region from the Qaidam Basin to WMQ. However, the wave propagation along our profile may be slightly up-dip, so crustal thickness should be considered a lower bound, while P_n velocity (8.0 km/s) is an upper estimate.

Synthetic frequency-wavenumber integration seismograms are plotted on the right sides of Figures 18 and 19. The source parameters assumed are listed in Table 3. These include Harvard CMT mechanisms (PDE) when available; otherwise an average thrust mechanism is assumed. Once again, the source corner frequency has little effect, so the synthetics are simply bandpassed from the ground displacement impulse response computed to 4 Hz. For these profiles, source depth is assumed to be 20 km. In Figure 18, only P_n, P_g and S_g (or L_g) are identifiable, and the synthetics provide a reasonable agreement in character to the observed waveforms. In Figure 19, the travel-time curves P, P_n, P_MP, and the surface reflections of P_n and P_MP are plotted. This is not to suggest a one-to-one correspondence of arrivals, but simply to suggest which phases are predicted to arrive between P_n and P_g. At the closest sources, P and S are the largest amplitude arrivals. The Moho critical distance is about 110 km, so P_MP becomes a significant arrival shortly beyond this range. At the largest ranges (700 km and beyond), the P_{nl} wavetrain consists of a series of low-amplitude arrivals. In the synthetics, P_g begins with the direct P wave travelling nearly horizontally through the crust. At the largest ranges, the observed P_g is more emergent, undoubtedly due to scattering and lateral heterogeneity in the crust.

Comparisons of observed seismograms for each event with synthetics computed at 10, 20 and 30 km are shown in Figures 21-24. The observed displacements for events 88273 and 88320 (both 239 km, Figures 21 and 22) are very simple, with a large arrival preceded by a small phase that forms a shoulder on the first peak. In our model, these events are beyond critical range, so the small first arrival is P_n. The large arrival is likely a combination of the direct P wave, P_CP and P_MP, all of which arrive close together for a shallow source. In the synthetics, however, P_n is distinct from this larger arrival, suggesting that the critical range in our model should be at slightly larger range. The synthetics also predict a large secondary arrival corresponding to sP_MP, which moves out with source depth. For event 88320 (Figure 22), if the arrival observed at about 12-13 sec corresponds to this phase, the source depth must be less than 10 km. Similarly, the arrival observed between this phase and the first arrival may be pP_n or pP_MP, so we interpret the source depth to be about 7-8 km (denoted by the arrow; the PDE depth is 33 km). Event 88273 (Figure 21) has no distinct observed secondary arrivals, but the coda following the first arrival has a duration of 5-6 sec. If this coda consists of the surface-reflected phases, the source of this event must be shallower than 10 km as well.

P_n for event 87356 (317 km, Figure 23) is emergent and very difficult to identify. Perhaps appropriately, the synthetics for this event contain some wrap-around, so P_n is difficult to identify in the synthetics as well. The first substantial arrivals predicted consist of a combination of P_MP and the direct P wave. If we align the synthetics on the predicted P_n arrival and align these larger arrivals with the first series of large arrivals in the observed waveform, we may identify some of the later arrivals. The PDE depth for this event is 21 km (denoted by the arrow). At this depth, the second sequence of arrivals (beginning at about 18 sec) is the second crustal multiple, $(P_MP)_2$. pP_MP may be interpreted as the relatively low-frequency arrival between these two sequences of arrivals.

The first arrival from event 87056 (700 km, Figure 24) is easily identified as P_n, but the observed waveform is much more complicated than the synthetics. This is particularly the case for the direct P wave, which is large and distinct in the synthetics, but difficult to identify in the observed record. This is not surprizing, since the horizontally traveling P wave to a range of 700 km encounters substantial scattering and lateral variations that are not included in the plane-layered structure model of the synthetics. Nevertheless, if we identify the first arrival as P_n, the secondary arrival at about 16 sec as P_MP and the envelope of arrivals beginning at about 22-23 sec as the combination of P with the crustal multiples, we find that these arrival times are consistent with the PDE depth of 26 km (denoted by the arrow).

CONCLUSIONS AND RECOMMENDATIONS:

Broad-band P_n-P_g waveforms from earthquakes at regional distances recorded at station WMQ in western China can be well modeled using frequency-wavenumber integration synthetics and plane-layered velocity structure models. Although not a primary purpose of this study, we have developed velocity structure models appropriate for regional wave propagation from three azimuths toward WMQ. Common features include a near-surface velocity gradient (modeled as a lower velocity layer), a fairly constant velocity (6.0 - 6.25 km/s) through most of the crust, a lower-crustal layer or gradient, and a relatively thick crust (48 - 59 km). The model for the profile of earthquakes SSE of WMQ has a thinner crust (48 km) than that for the NNE profile (59 km), which is consistent with the observation of Mangino and Ebel (1992) that the Moho dips to the NNW at WMQ. On the other hand, our models (and others from nearby regions, such as Quin and Thurber, 1992) based on regional P-wave modeling have a much larger velocity contrast at the Moho than the teleseismic receiver function models of Mangino and Ebel (1992).

Broad-band P_n-P_g waveforms at ranges up to 1000 km are result from the interference of a variety of phases. Since some of these depart upward from the source and others depart downward, this interference pattern is quite sensitive to source depth. This study has shown that, in addition, the interference pattern is also dependent on radiation pattern, since the important phases in the P_n-P_g waveform are different for different azimuths and different mechanisms. For the SW profile, waves that begin as upward-departing S waves (e.g., sP_n, sP_MP) dominate the waveform. For the NNE and SSE profiles, direct P and crustal multiples (P_MP, $(P_MP)_2$) seem to be most important. What this means is that if accurate Green's functions can be computed (and Green's functions are only as accurate as the velocity structure model assumed), regional P_n-P_g waveforms can provide excellent discrimination for source depth and mechanism. In order to be applied to nuclear event discrimination, it will be necessary to "calibrate" a region, by determining a velocity structure model and comparing synthetic and observed waveforms for a source with known depth and mechanism. Thereafter, the Green's functions for that path can serve to discriminate earthquakes from explosions.

REFERENCES:

Barker, J.S. (1984). A seismological analysis of the 1980 Mammoth Lakes, California, earthquakes, *PhD Thesis*, Pennsylvania State Univ.

Barker, J.S. (1991). Analysis of regional bodywave phases from earthquakes and explosions in eastern Asia, Papers Presented at 13th annual PL/DARPA Seismic Research Symposium, Keystone, CO, *PL-TR-91-2208*, 64-70, ADA241325.

Bennett, T.J., J.F. Scheimer, A.K. Campanella and J.R. Murphy (1990). Regional discrimination research and methodology implementation: Analyses of CDSN and Soviet IRIS data, *Scientific Report No. 4, GL-TR-90-0194*, Air Force Geophysics Laboratory, ADA230251.

Burdick, L.J., C.K. Saikia and D.V. Helmberger (1989). Deterministic modeling of regional waveforms from the Nevada Test Site, *Final Report, GL-TR-89-0196*, Air Force Geophysics Laboratory, ADA216641.

Burdick, L.J., C.K. Saikia, J.P. McLaren, L.S. Zhao and D.V. Helmberger (1992). Specialized studies in yield estimation, *Final Report, PL-TR-92-2070*, Phillips Laboratory, ADA254344.

Feng, C.C. and T.L. Teng (1983). Three dimensional crust and upper mantle structure of the Eurasian continent, *J. Geophys. Res., 88*, 2261-2272.

Helmberger, D.V. and D.G. Harkrider (1978). Modeling earthquakes with generalized ray theory, in *Proc. IUTAM Symp.: Modern Problems in Elastic Wave Propagation*, J. Miklowitz and J. Achenback, eds., Wiley.

Hu F., Hu J., Bai M., Chen S., Zhou D. and Liu J. (1989). Seismotectonics of Xinjiang Uygur Autonomous Region, in *Lithospheric Dynamics Atlas of China*, Ma Xingyuan, chief editor, China Cartographic Publishing House, Beijing, 57.

Mangino, S. and J. Ebel (1992). The receiver structure beneath the Chinese Digital Seismograph Network (CDSN) stations: Preliminary results, *Scientific Report No., 1, PL-TR-92-2149,* Phillips Laboratory, ADA256681.

Saikia, C.K. and L.J. Burdick (1991). Fine structure of Pnl waves from explosions, *J. Geophys. Res., 96,* 14,383-14,401.

Shi Z., Liu Z. and Yin X. (1989). Crustal Thickness by Gravity Inversion, in *Lithospheric Dynamics Atlas of China,* Ma Xingyuan, chief editor, China Cartographic Publishing House, Beijing, 12.

State Seismological Bureau (1986). *Results of Geophysical Exploration of the Crust and Upper Mantle in China,* Beijing.

Quin, H.R. and C.H. Thurber (1992). Seismic velocity structure and event relocation in Kazakhstan from secondary P phases, *Bull. Seism. Soc. Am., 82,* 2494-2510.

Wu, F.T. (1990). Studies of regional phases and discriminants in Asia, *Final Report, GL-TR-90-0017,* Air Force Geophysics Laboratory, ADA222184.

Wu, F.T. and J.S. Barker (1992). Studies of regional body and surface waves in eastern Asia - Data analysis and modeling, *Scientific Report No. 1, PL-TR-92-2171,* Phillips Laboratory.

Wu. F.T. (1993). Surface wave group velocity tomography of east Asia, *Final Report (Part I), PL-TR-93-2102(I),* Phillips Laboratory.

Zhao, L.S. and D.V. Helmberger (1991). Broadband modeling along a regional shield path, Harvard recording of the Saguenay earthquake, *Geophys. J. Int., 105,* 301-312.

Table 1 - Earthquakes Recorded at WMQ

Date	Time (GMT)	Lat. (°N)	Lon (°E)	R (km)	Az (°)	Depth (km)	m_b
SW Profile							
10/6/87 (87279)	1306:20.3	43.44	88.55	82.0	302	32	4.8
12/17/87 (87351)	1217:25.0	41.94	83.20	421.9	59	33*	5.1
8/5/87 (87217)	1024:21.0	41.36	82.11	534.1	57	33*	4.8
1/5/87 (87005)	2252:46.5	41.96	81.32	559.6	66	17	5.9
1/24/87 (87024a)	0809:21.0	41.53	79.32	731.2	67	29	5.9
1/24/87 (87024b)	1340:40.0	41.44	79.25	740.5	66	33*	5.2
6/8/87 (87159)	1330:36.0	39.79	74.69	1175.0	63	10	5.1
4/30/87 (87120)	0517:37.0	39.76	74.57	1178.3	63	8	5.7
NNE Profile							
10/6/87 (87279)	1306:20.3	43.44	88.55	82.0	302	32	4.8
9/18/87 (87261)	2159:15.0	47.02	89.66	387.6	204	33*	5.3
4/1/88 (88092)	0127:16.0	47.53	89.64	439.4	201	10	4.6
7/23/88 (88205)	0738:9.7	48.71	90.56	586.4	203	19	5.5
6/30/88 (88182)	1525:15.5	50.23	91.14	759.4	202	33*	5.0
9/16/87 (87259)	1759:30.6	52.09	95.70	1095.5	216	33*	4.8
SSE Profile							
10/6/87 (87279)	1306:20.3	43.44	88.55	82.0	302	32	4.8
9/29/88 (88273)	0700:3.1	41.75	88.47	238.9	345	33*	4.7
11/15/88 (88320)	1656:46.2	42.02	89.30	239.4	327	33*	5.0
12/22/87 (87356)	0016:39.04	41.36	89.64	316.9	330	21	5.9
2/25/87 (87056)	1957:52.0	38.10	91.18	699.9	336	26	5.7
12/6/87 (87340)	1620:44.9	37.39	94.52	917.8	323	33*	4.7

* Depth uncertain. 33 km is the PDE default.

Compiled from PDE, Wu (1990), and Bennett et al. (1990).

Table 2 - Velocity Structure Models

V_P (km/s)	V_S (km/s)	Density (g/cm^3)	Thickness (km)	Q_P	Q_S
SW Profile (Tienshan and Tarim Basin)					
4.80	2.77	2.58	9.0	300	150
6.25	3.61	2.79	32.0	800	400
7.25	4.18	3.00	15.0	1000	500
8.00	4.62	3.33	20.0	1200	600
8.10	4.68	3.36	20.0	1200	600
8.20	4.73	3.40	40.0	1200	600
8.30	4.79	3.45	h.s.	1200	600
NNE Profile (Altai Mountains)					
4.80	2.77	2.58	5.0	300	150
6.00	3.46	2.79	42.0[1] 45.0[2] 52.0[3]	800	400
6.90	4.00	2.85	4.0[1] 3.0[2] 4.0[3]	1000	500
7.40	4.27	3.00	1.0[1] 6.0[2] 1.0[3]	1000	500
8.15	4.70	3.20	10.0	1200	600
8.26	4.77	3.30	h.s.	1200	600
SSE Profile (near Lop Nor)					
4.80	2.77	2.58	12.0	300	150
6.25	3.78	2.79	26.0	1000	500
6.80	3.93	2.85	10.0	1000	500
8.00	4.62	3.34	10.0	1200	600
8.10	4.68	3.36	h.s.	1200	600

[1] Assuming a source depth of 10 km.
[2] Assuming a source depth of 20 km.
[3] Assuming a source depth of 30 km.

Table 3 - Source Parameters for the Synthetics

Date	R (km)	Az (°)	Strike (°)	Dip (°)	Rake (°)	M_0 ($\times 10^{23}$ dyne-cm)	f_c[c] (Hz)
SW Profile							
87279	82	302	220[b]	40[b]	65[b]	30.[b]	
Syn2	200	60	220[b]	40[b]	65[b]	30.[b]	
87351	422	59	220[b]	40[b]	65[b]	30.[b]	0.5
87217, 87005	560	66	226[a]	21[a]	47[a]	41.[a]	0.8
87024a, 87024b	740	67	268[a]	45[a]	107[a]	200.[a]	0.8
Syn6	950	60	220[b]	40[b]	65[b]	30.[b]	
87159	1175	63	298[a]	27[a]	91[a]	6.5[a]	0.3
NNE Profile							
87279	82	302	120[b]	90[b]	180[b]	1.8[b]	
Syn2	200	200	120[b]	90[b]	180[b]	1.8[b]	
87261, 88091	400	200	154[a]	90[a]	180[a]	1.3[a]	
88205	586	203	331[a]	66[a]	170[a]	9.0[a]	
88182	759	201	152[a]	50[a]	-50[a]	3.5[a]	
Syn6	950	200	70[b]	70[b]	-40[b]	1.8[b]	
87259	1095	216	70[b]	70[b]	-40[b]	1.8[b]	
SSE Profile							
87279	82	302	270[b]	60[b]	70[b]	1.8[b]	
Syn2	160	330	270[b]	60[b]	70[b]	1.8[b]	
88273, 88320	240	330	270[b]	60[b]	70[b]	1.8[b]	
87356	317	330	316[a]	53[a]	54[a]	2.1[a]	
Syn5	500	330	270[b]	60[b]	70[b]	1.8[b]	
87056	700	336	267[a]	60[a]	68[a]	5.8[a]	
87340	918	323	270[b]	60[b]	70[b]	1.8[b]	

[a] Mechanisms are Harvard CMT solutions published in the PDE.
[b] No mechanism published. These values are assumed.
[c] If not specified, f_c is assumed to be > 4 Hz.

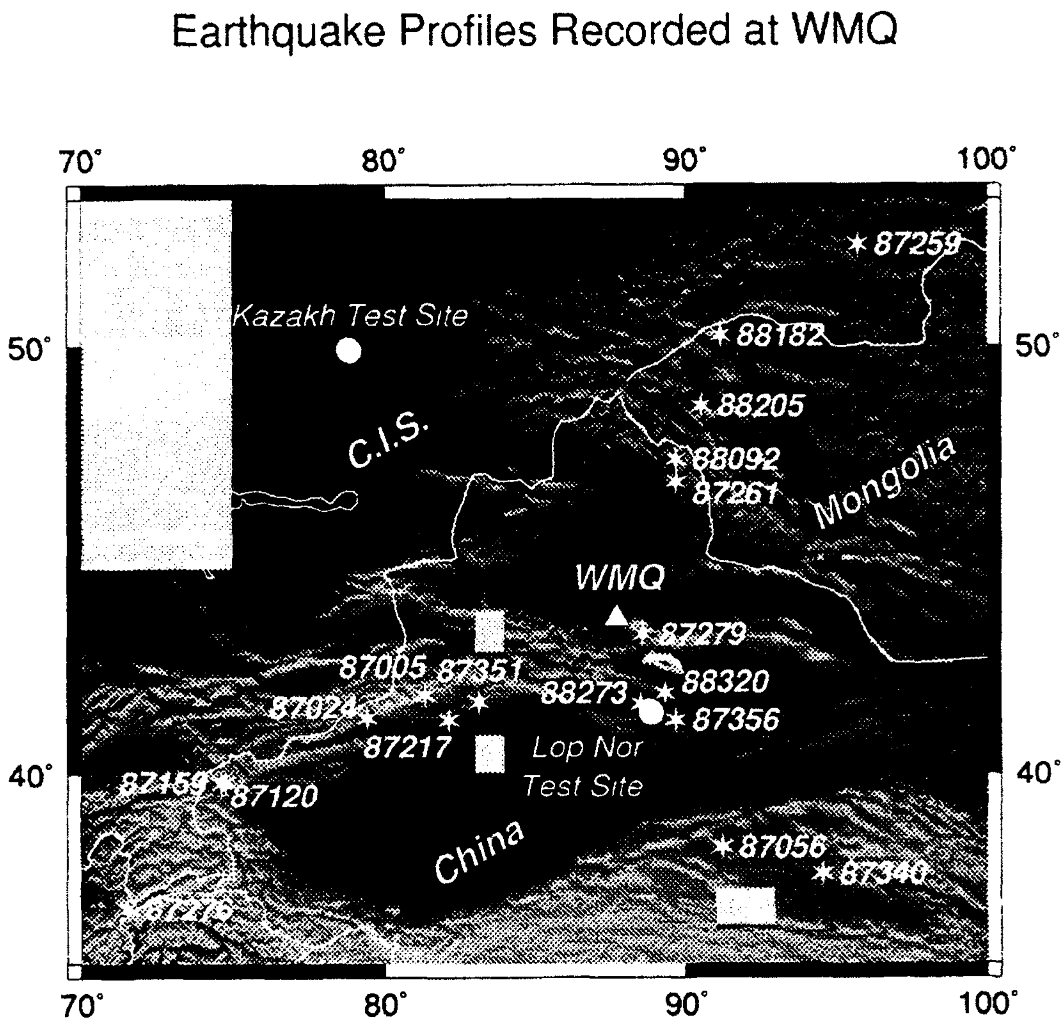

Fig. 1 - Shaded topographic map of the northwestern border region of China showing the locations of earthquakes (stars) recorded at CDSN station WMQ (triangle). Earthquakes SW, NNE and SSE of WMQ were modeled in this study (see Table 1). Also shown are the locations of the Kazakh test site and the Lop Nor test site (circles). Topography (courtesy of Eric Fielding, Cornell) is plotted with lighter shades indicating higher elevations. Gray squares indicate missing elevation data. The small gray oval SE of WMQ is the Turfan Basin, which is below sea level. The light region to the south is the edge of the Tibetan Plateau.

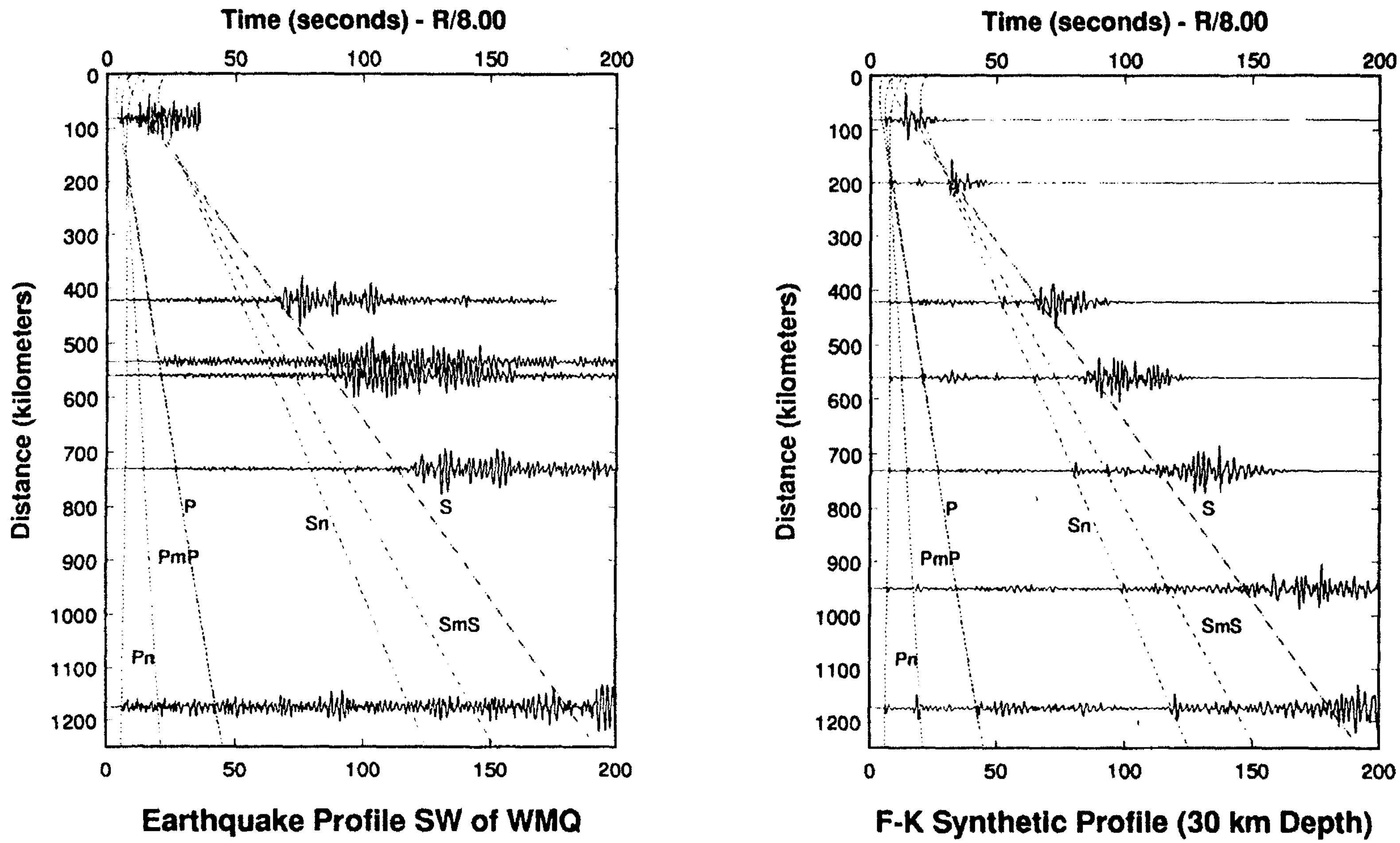

Fig. 2 - Profiles of observed (left) and frequency-wavenumber integration synthetic (right) vertical-component displacement waveforms for earthquakes from the SW recorded at CDSN station WMQ. Also shown are travel-time curves for important P- and S-wave phases computed for a source at 20 km depth in the velocity structure model listed in Table 2.

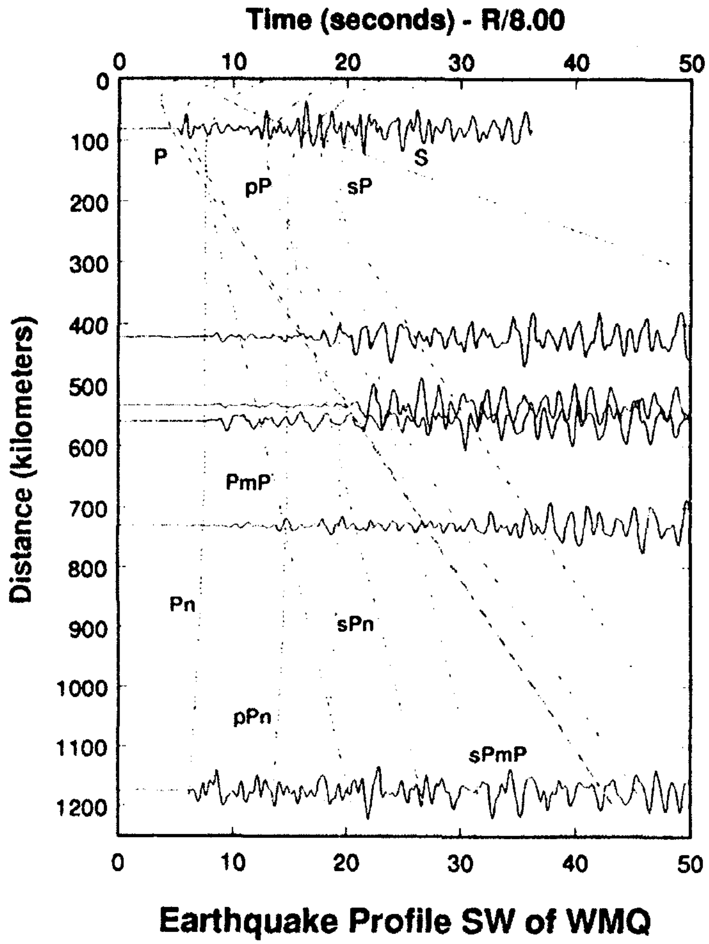

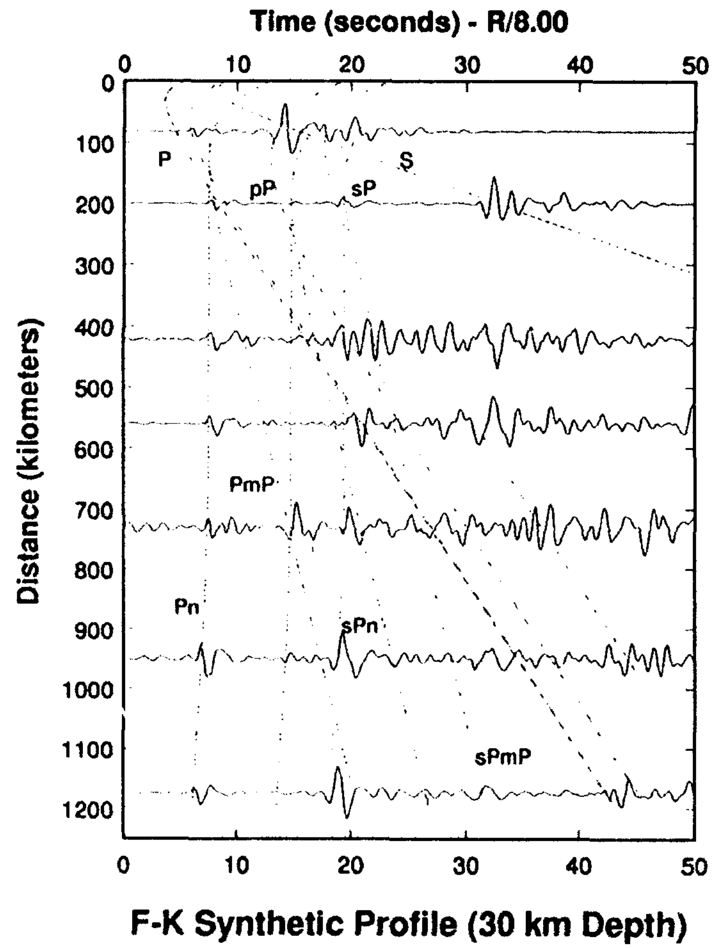

Fig. 3 - The first 50 sec of the observed (left) and synthetic (right) seismogram profiles shown in the previous figure. Shown are the P_n-P_g portions of the waveforms, along with travel-time curves for selected phases.

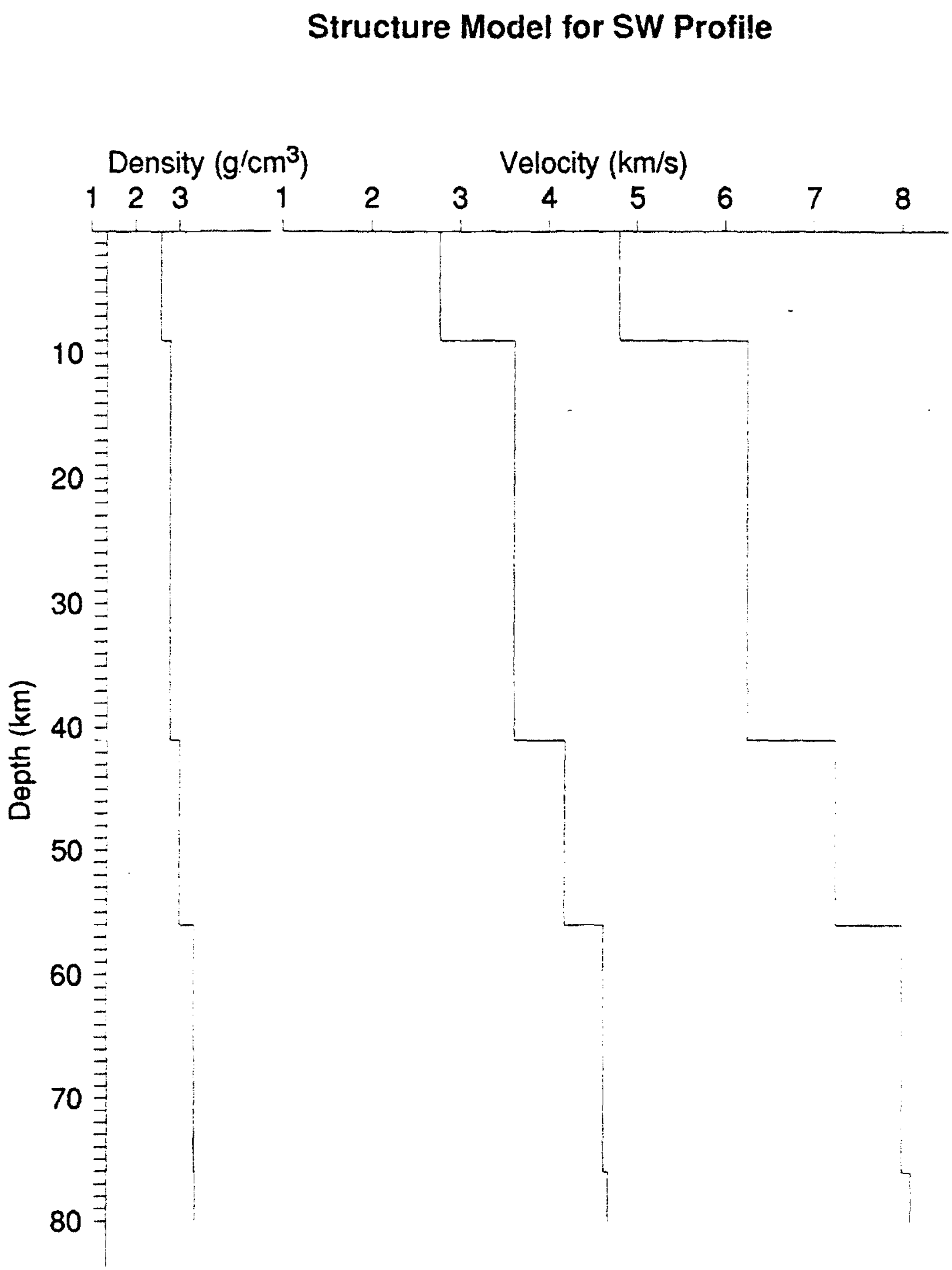

Fig. 4 - Velocity structure model for the profile SW of WMQ.

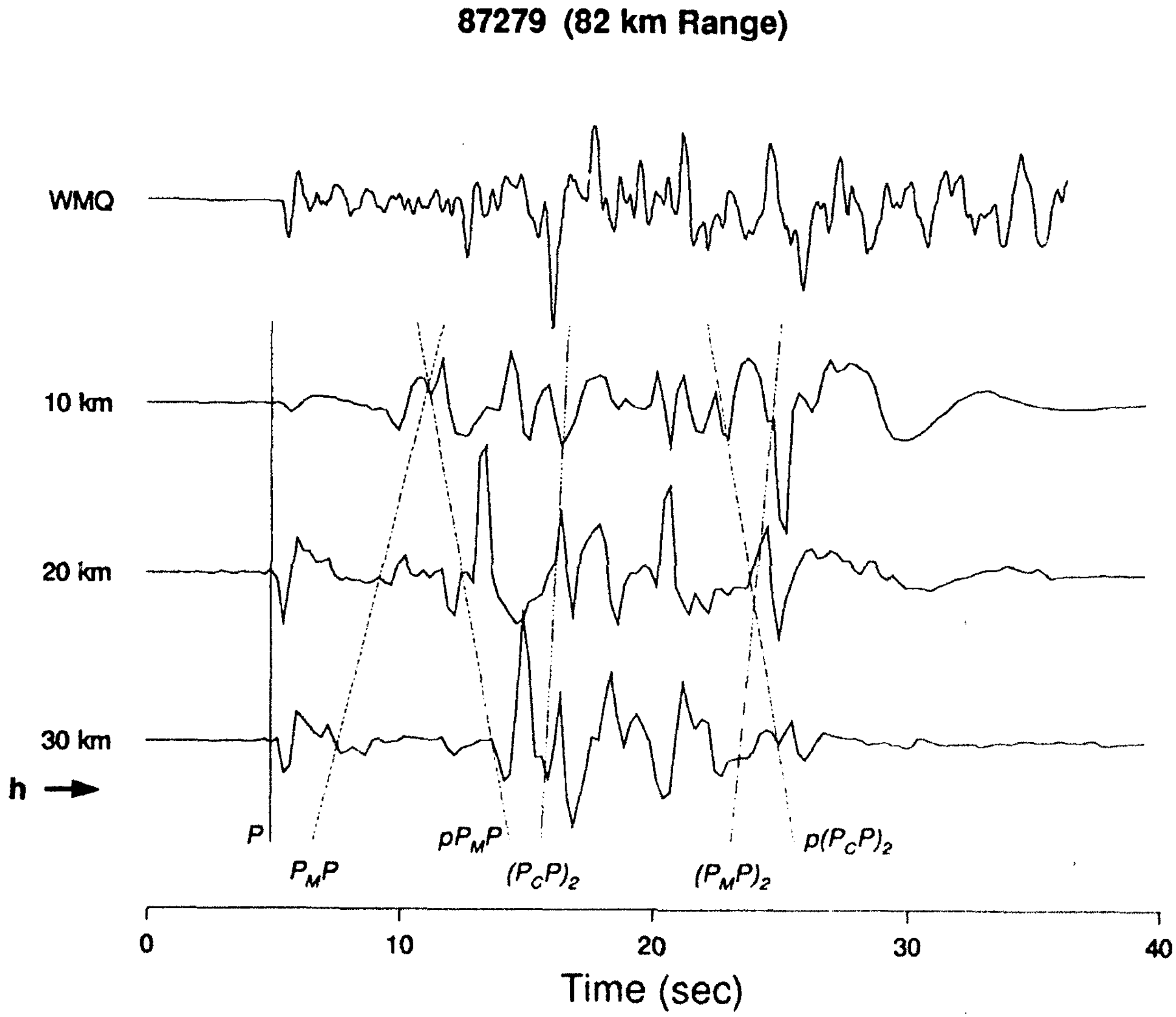

Fig. 5 - Comparison of the observed P_n-P_g waveform for event 87279 (top trace) with F-K synthetics computed for source depths of 10, 20 and 30 km. All traces are aligned on the P arrival. The moveout of significant phases (indicated by lines superimposed on the synthetics) changes the interference of arrivals. This enables a determination of source depth (denoted by the arrow labeled "h").

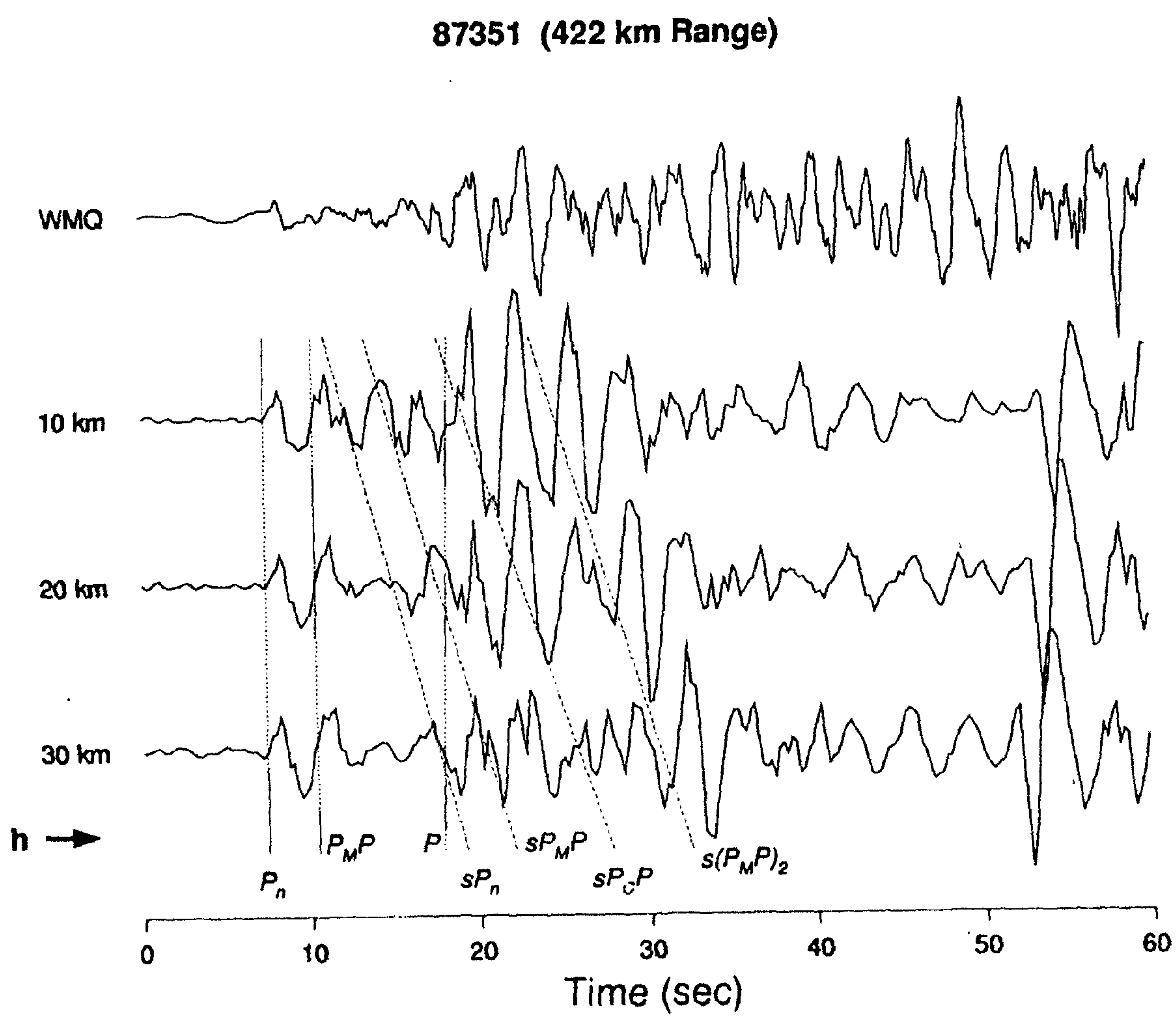

Fig. 6 - Comparison of the observed P_n-P_g waveform for event 87351 (top trace) with F-K synthetics computed for source depths of 10, 20 and 30 km. The format is the same as in Figure 5, except that the traces are aligned on the P_n arrival.

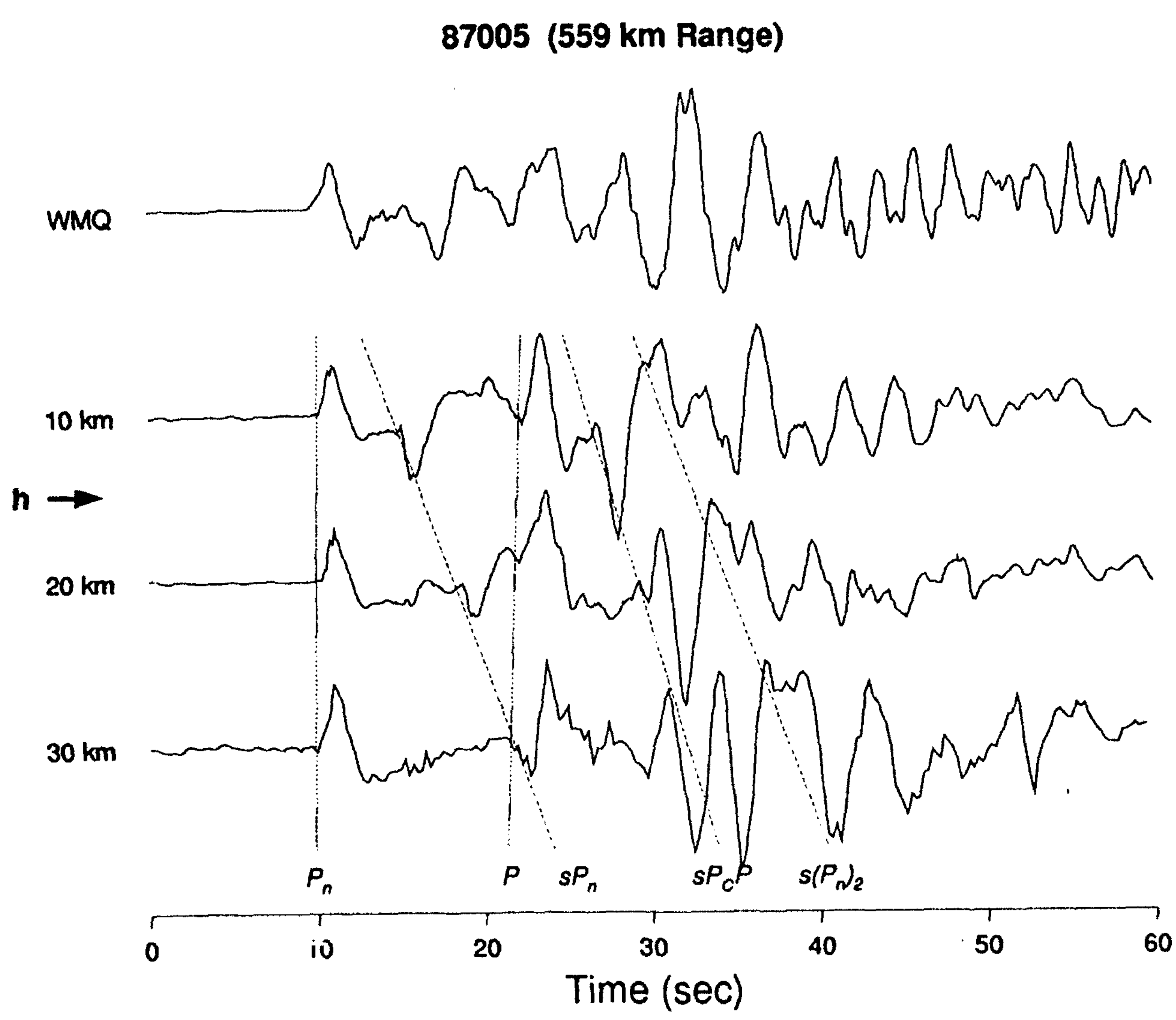

Fig. 7 - Comparison of the observed P_n-P_g waveform for event 87005 (top trace) with F-K synthetics computed for source depths of 10, 20 and 30 km. The format is the same as in Figure 6.

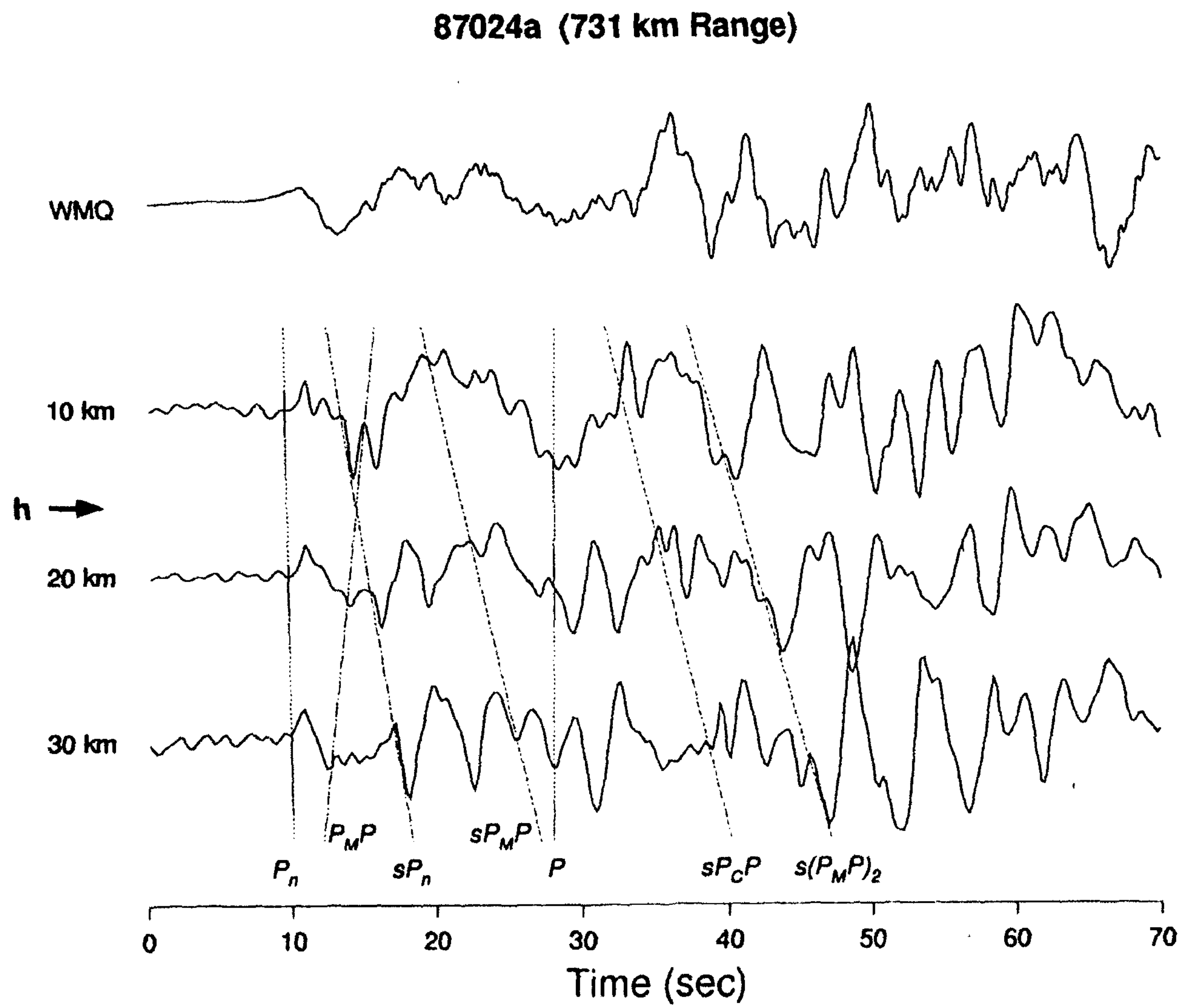

Fig. 8 - Comparison of the observed P_n-P_g waveform for event 87024a (top trace) with F-K synthetics computed for source depths of 10, 20 and 30 km. The format is the same as in Figure 6.

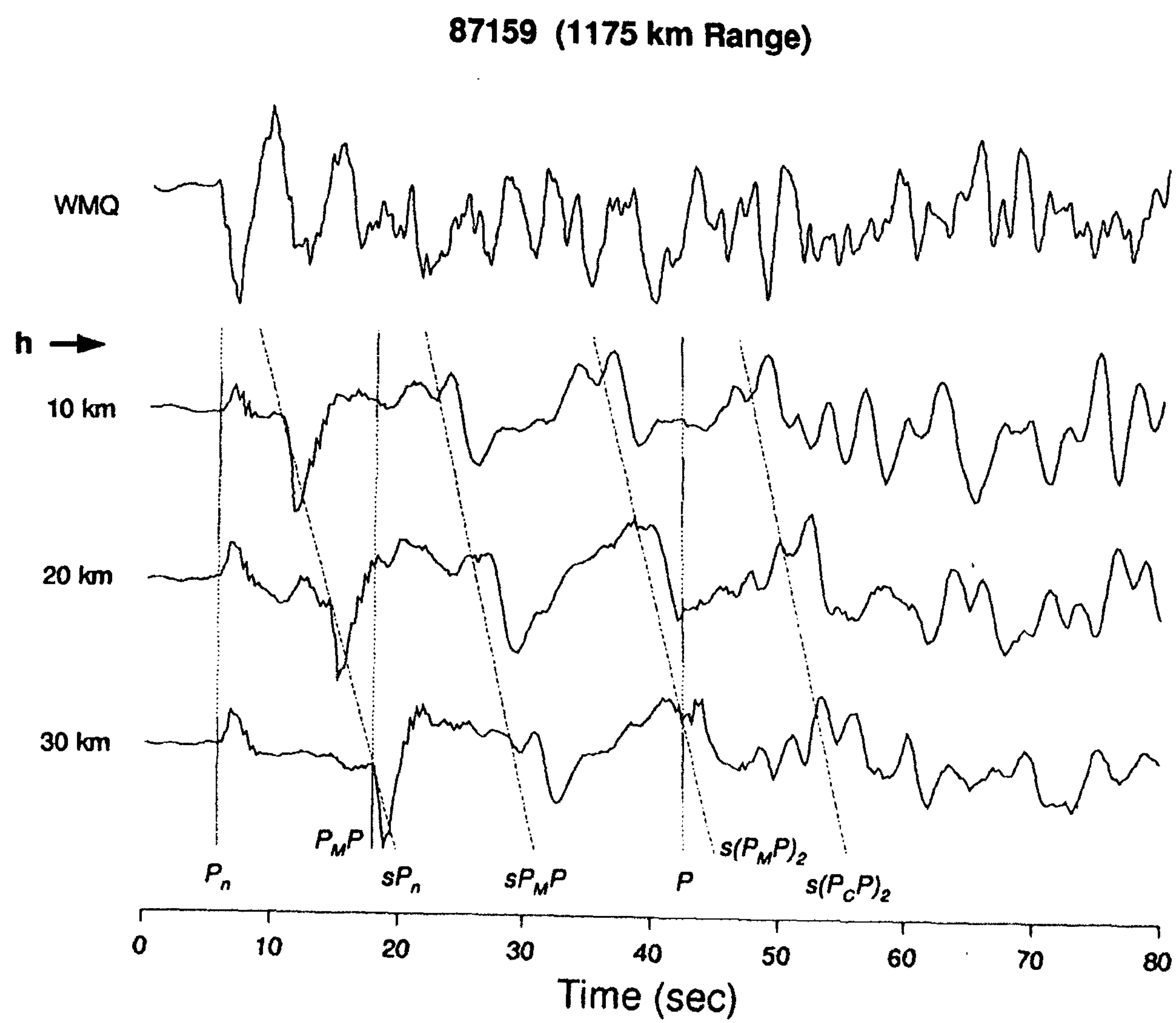

Fig. 9 - Comparison of the observed P_n-P_g waveform for event 87159 (top trace) with F-K synthetics computed for source depths of 10, 20 and 30 km. The format is the same as in Figure 6.

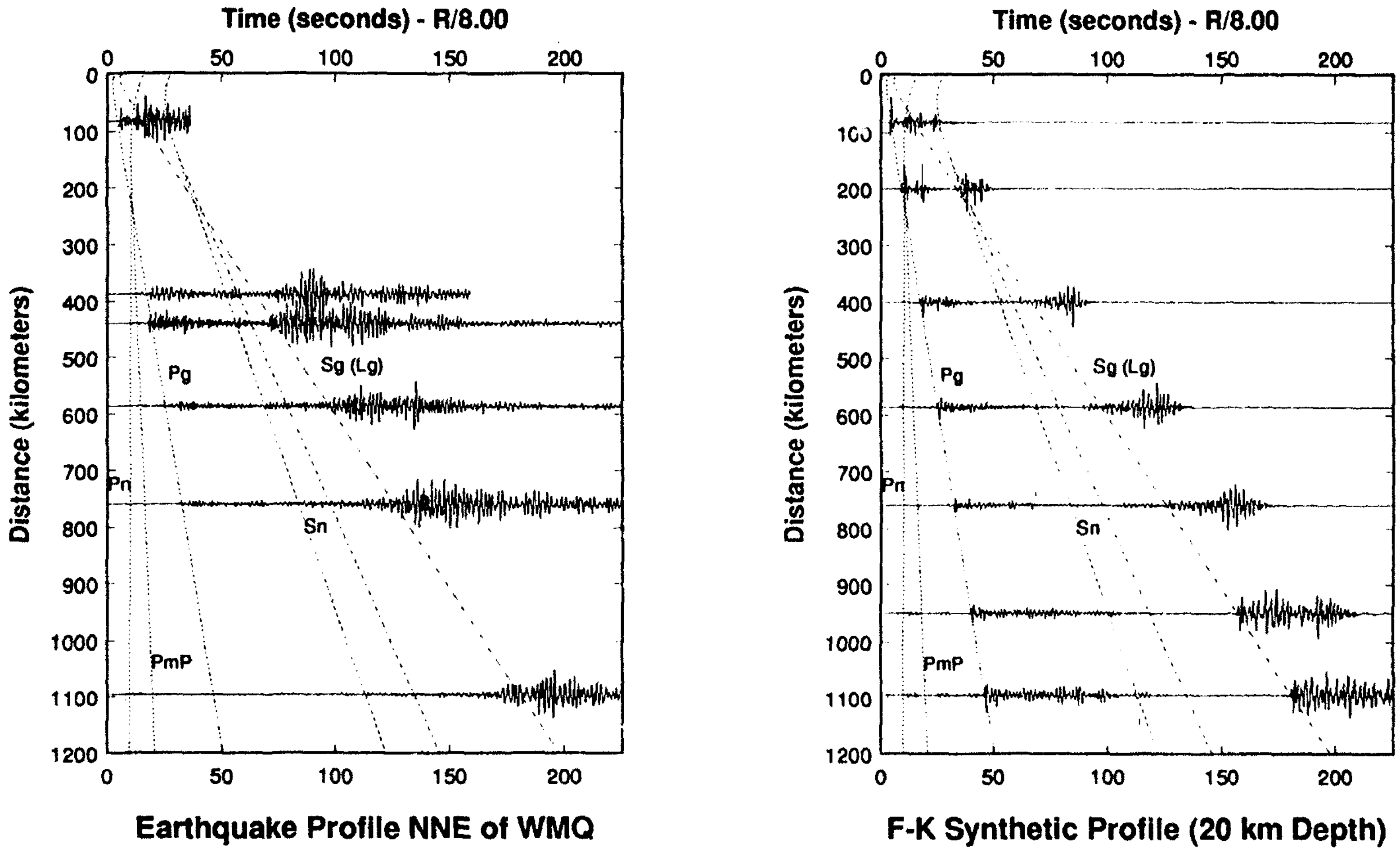

Fig. 10 - Profiles of observed (left) and synthetic (right) waveforms for earthquakes from the NNE recorded at WMQ. The format is the same as in Figure 2.

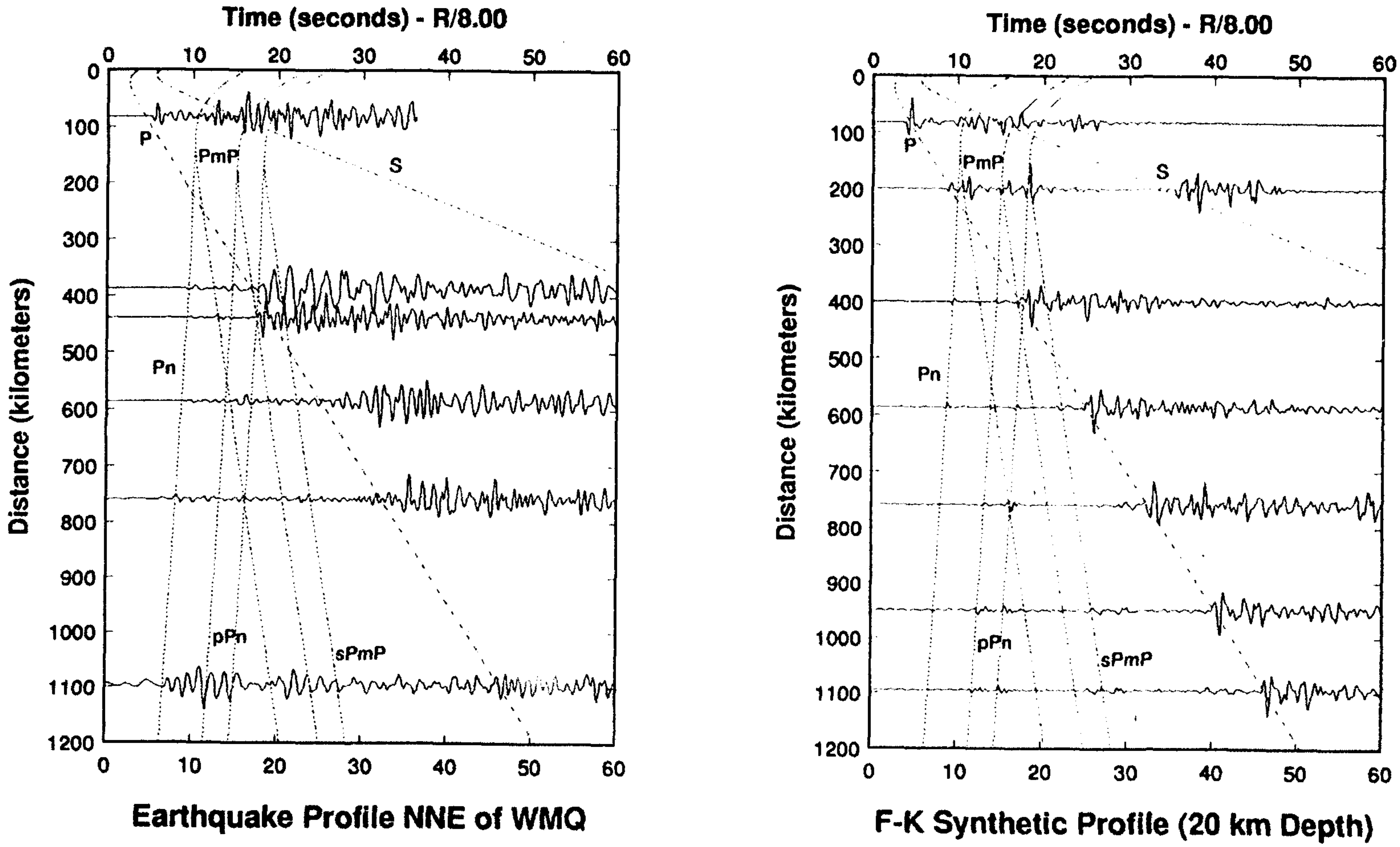

Fig. 11 - The P_n-P_g portions of the observed (left) and synthetic (right) seismogram profiles NNE of WMQ.

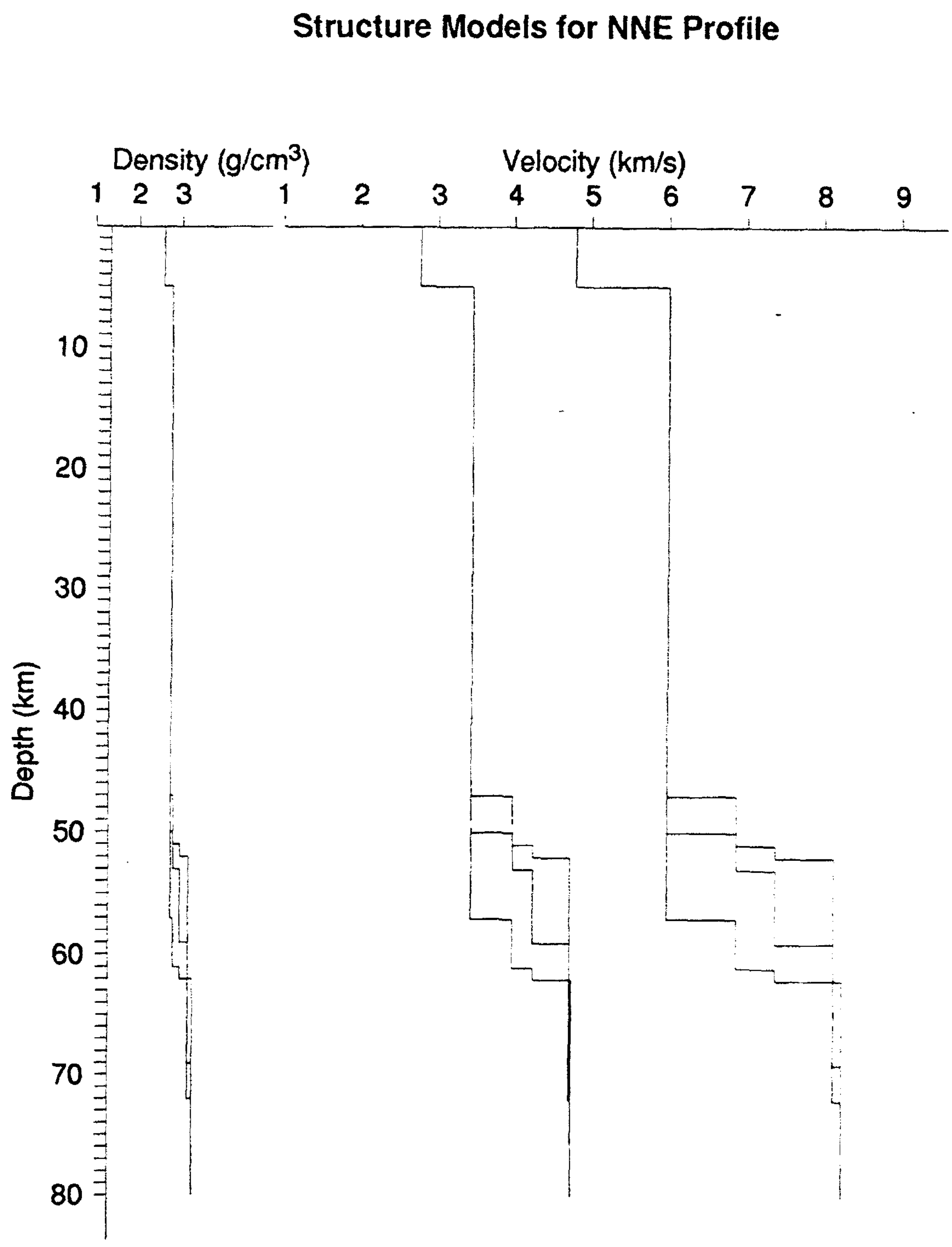

Fig. 12 - Velocity structure model for the profile NNE of WMQ.

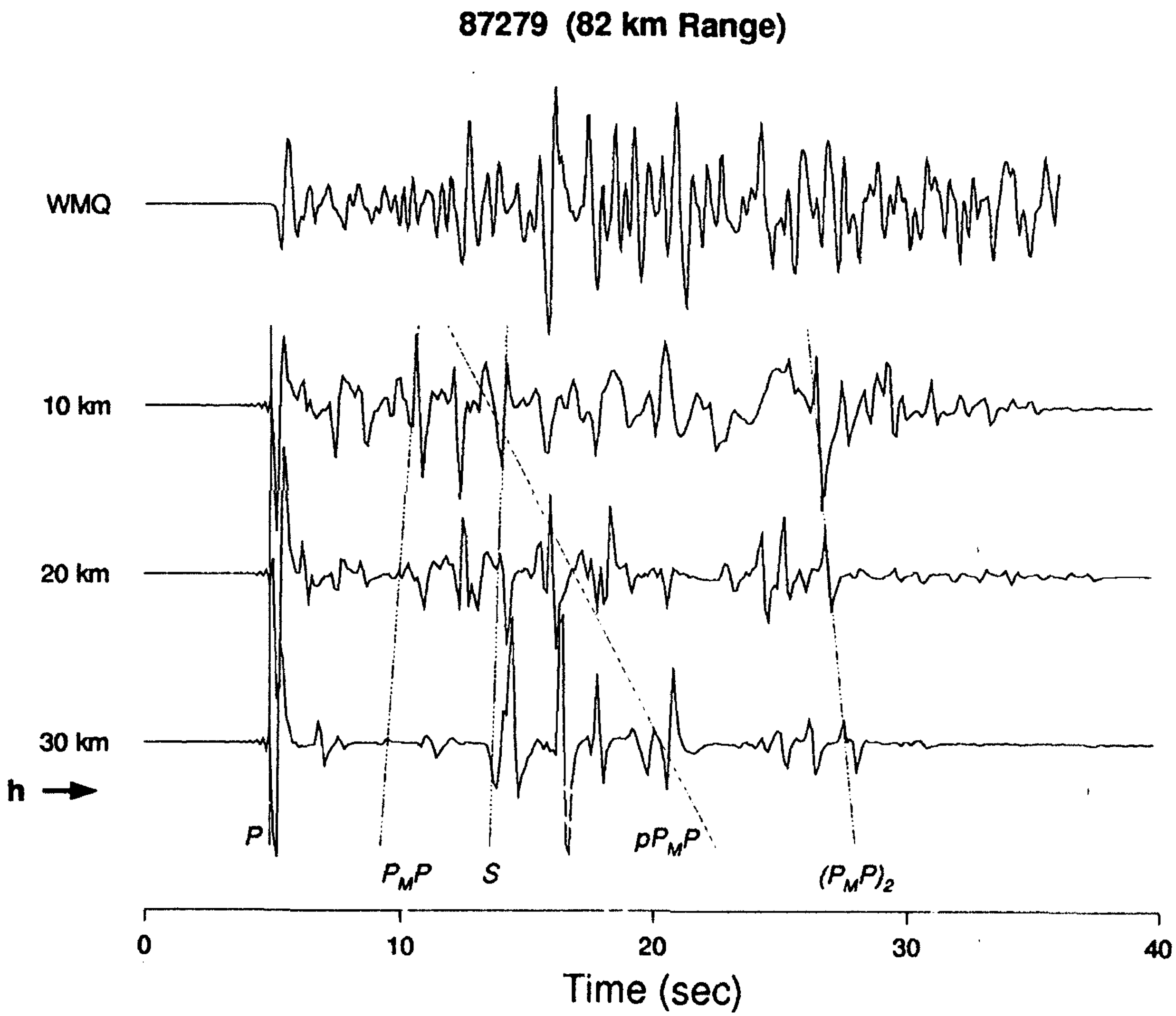

Fig. 13 - Comparison of the observed P_n-P_g waveform for event 87279 (top trace) with F-K synthetics computed for source depths of 10, 20 and 30 km. The format is the same as in Figure 5.

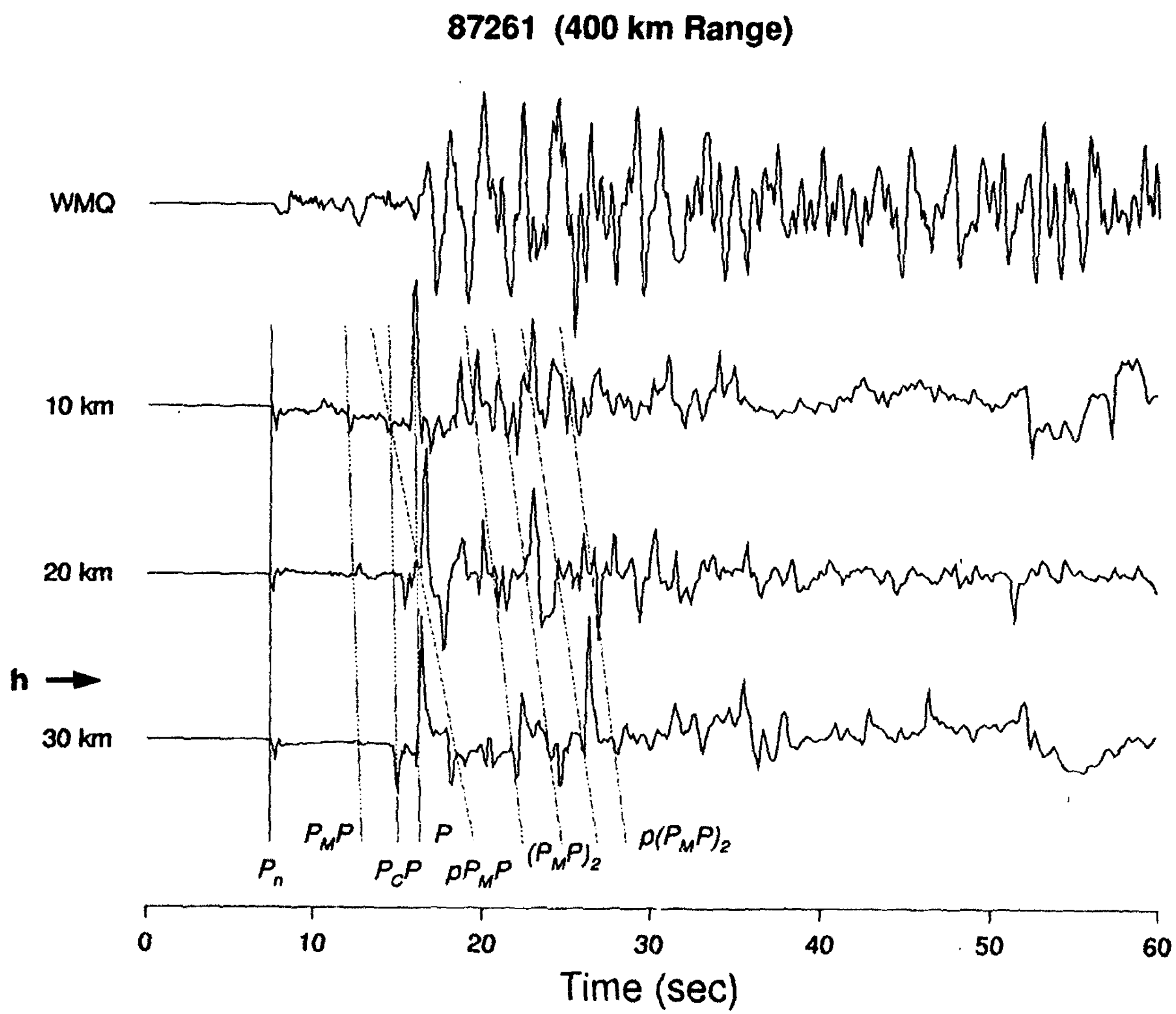

Fig. 14 - Comparison of the observed P_n-P_g waveform for event 87261 (top trace) with F-K synthetics computed at 400 km range for source depths of 10, 20 and 30 km. The format is the same as in Figure 6.

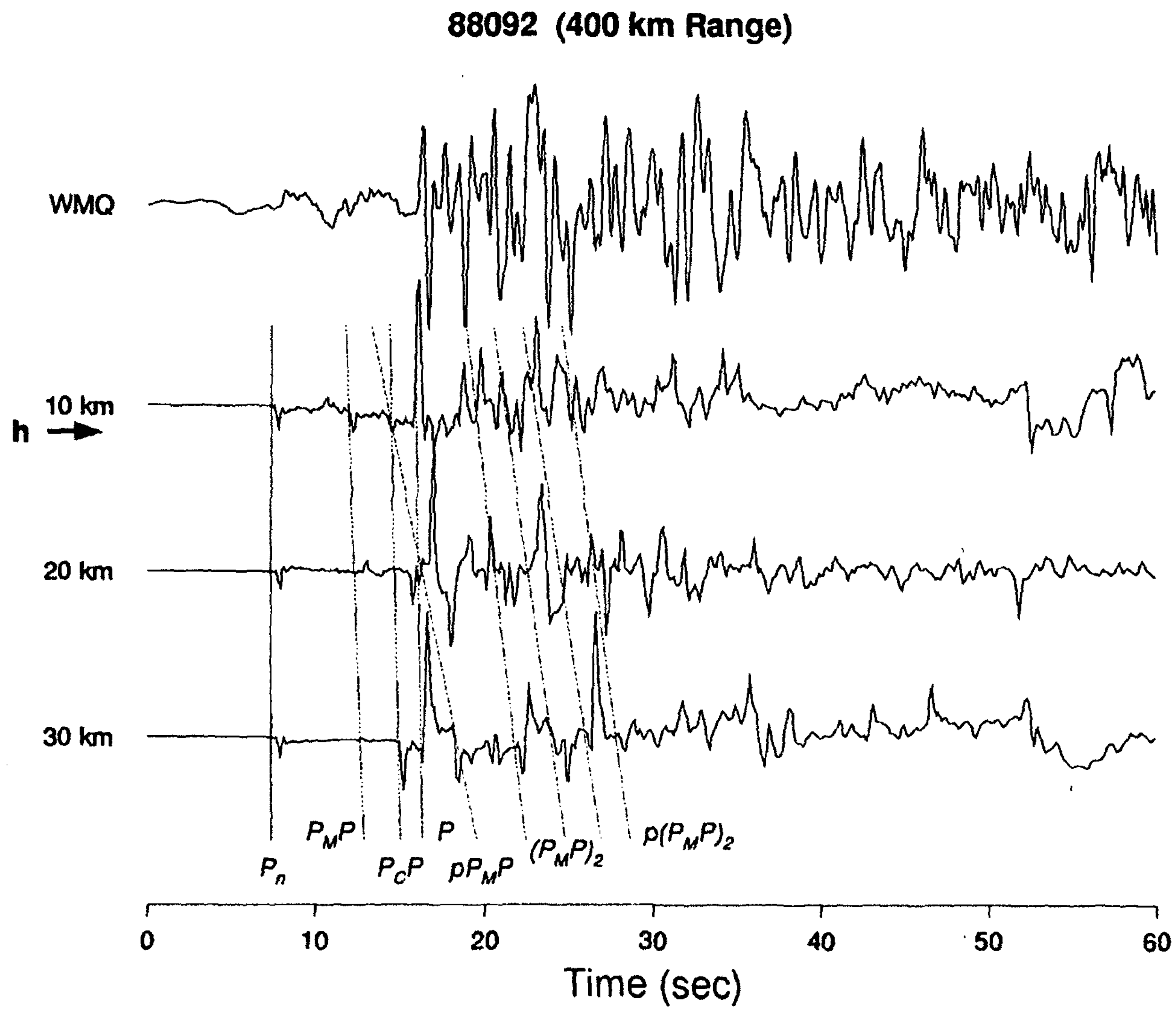

Fig. 15 - Comparison of the observed P_n-P_g waveform for event 88092 (top trace) with F-K synthetics computed at 400 km range for source depths of 10, 20 and 30 km. The format is the same as in Figure 6.

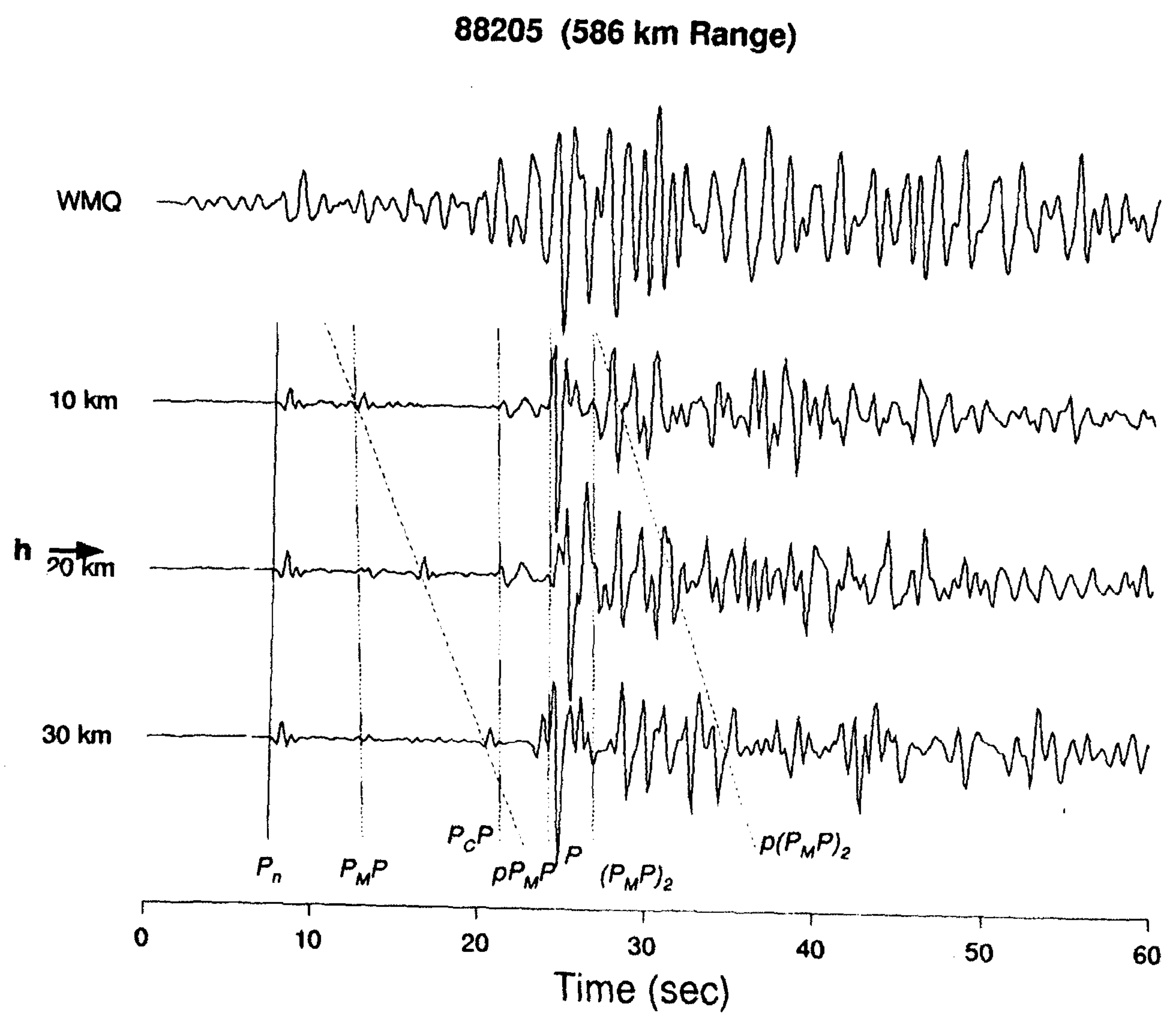

Fig. 16 - Comparison of the observed P_n-P_g waveform for event 88205 (top trace) with F-K synthetics computed for source depths of 10, 20 and 30 km. The format is the same as in Figure 6.

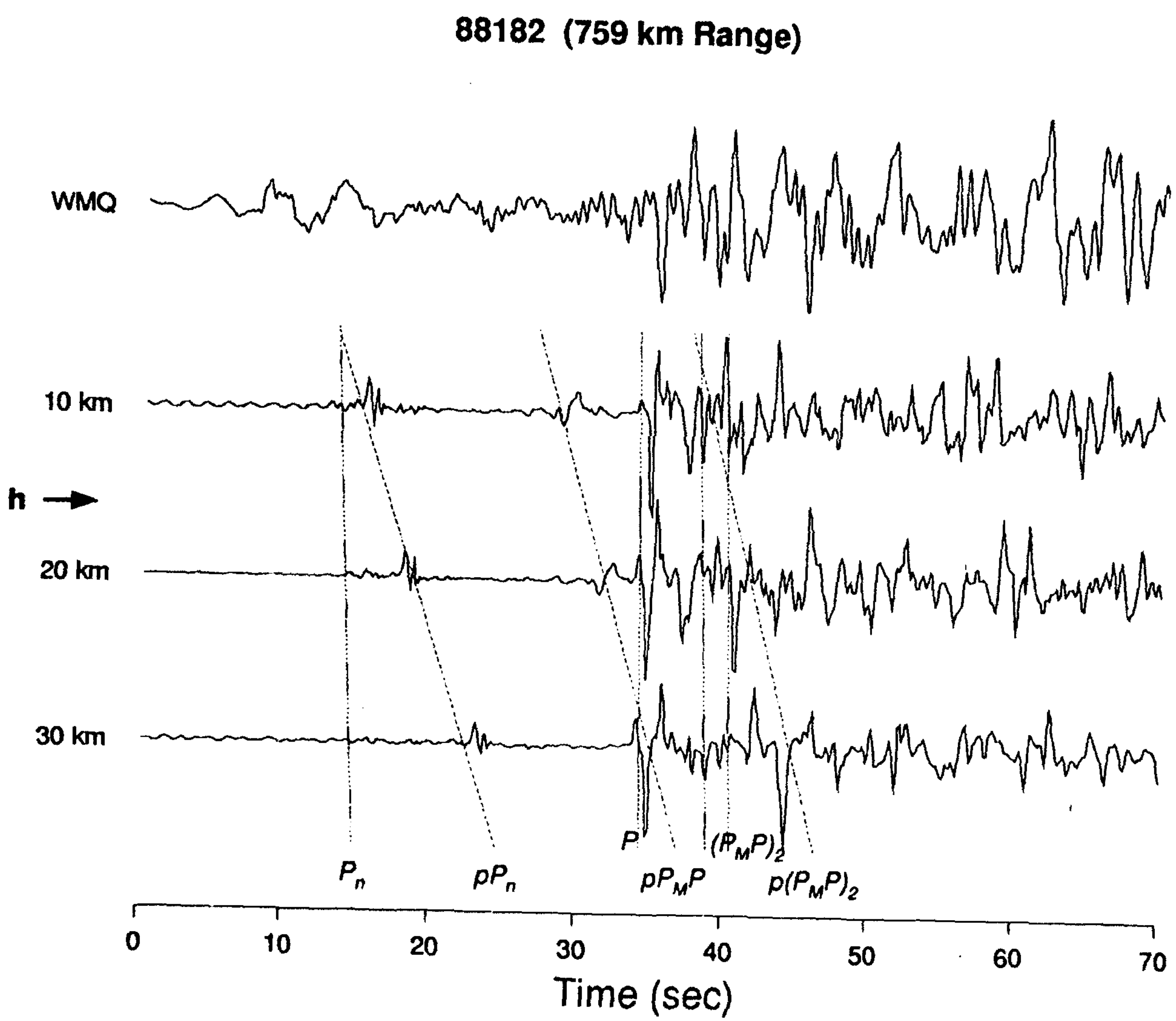

Fig. 17 - Comparison of the observed P_n-P_g waveform for event 88182 (top trace) with F-K synthetics computed for source depths of 10, 20 and 30 km. The format is the same as in Figure 6.

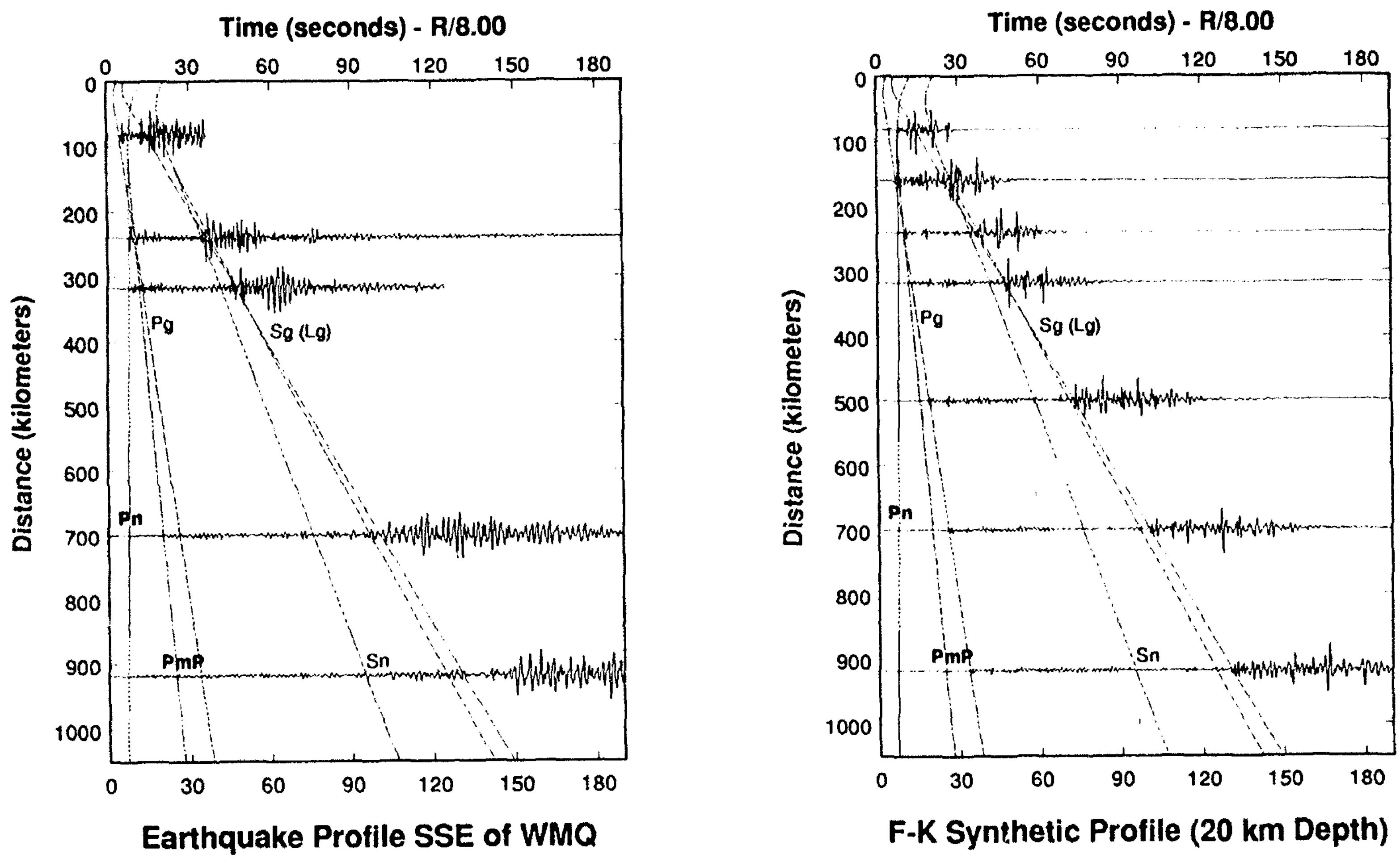

Fig. 18 - Profiles of observed (left) and synthetic (right) waveforms for earthquakes from the SSE recorded at WMQ. The format is the same as in Figure 2.

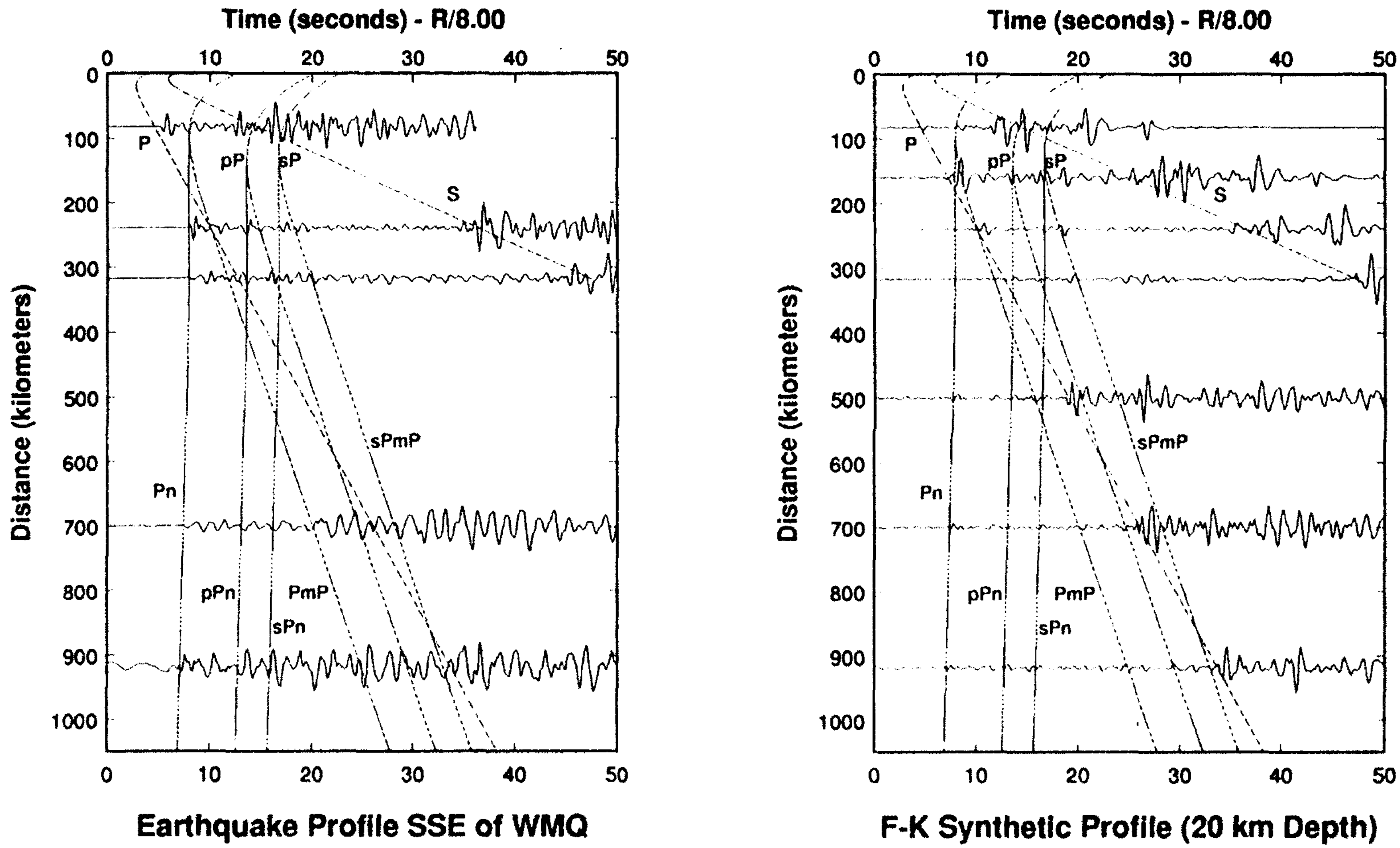

Fig. 19 - The P_n-P_g portions of the observed (left) and synthetic (right) seismogram profiles SSE of WMQ.

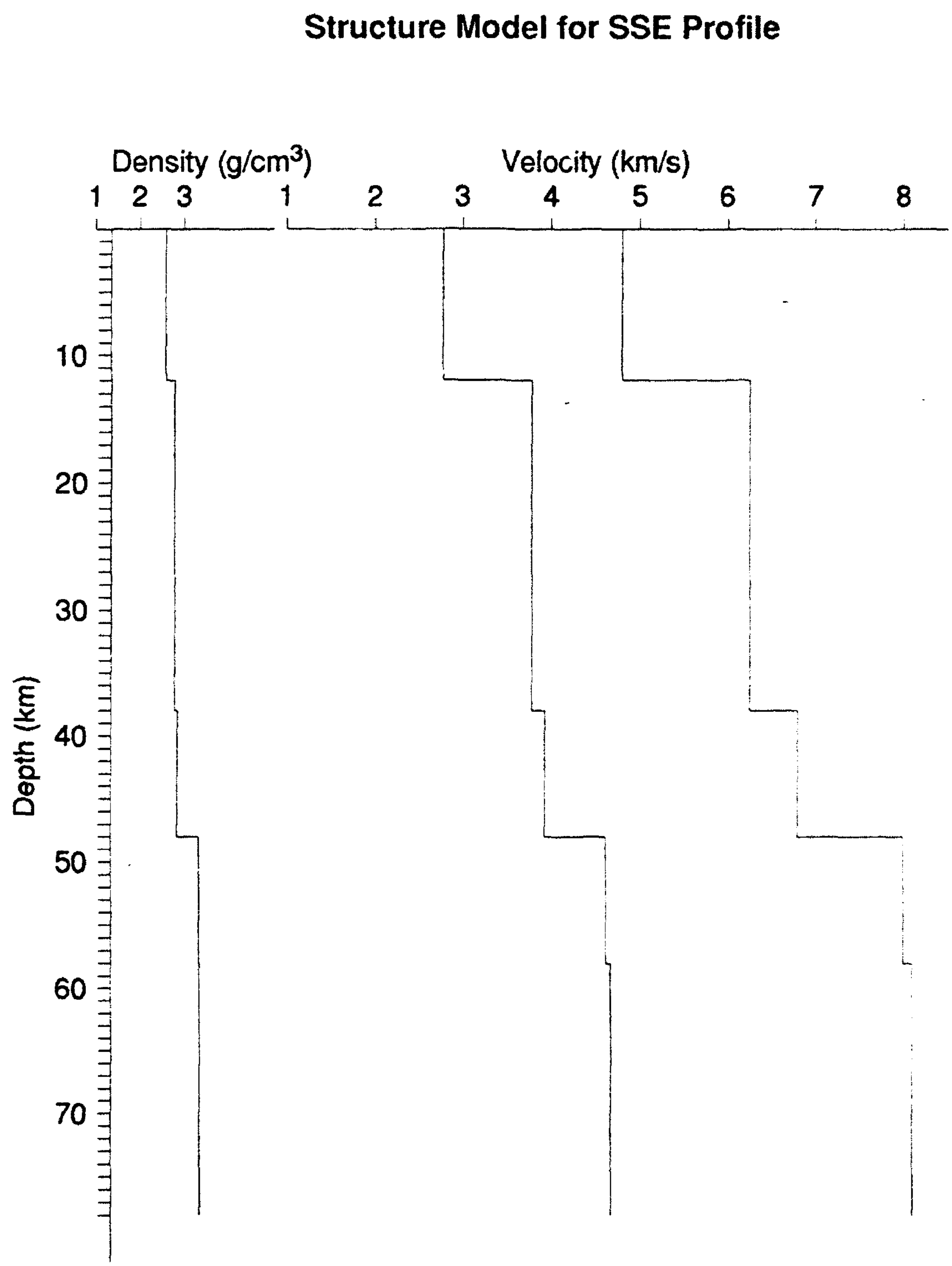

Fig. 20 - Velocity structure model for the profile SSE of WMQ.

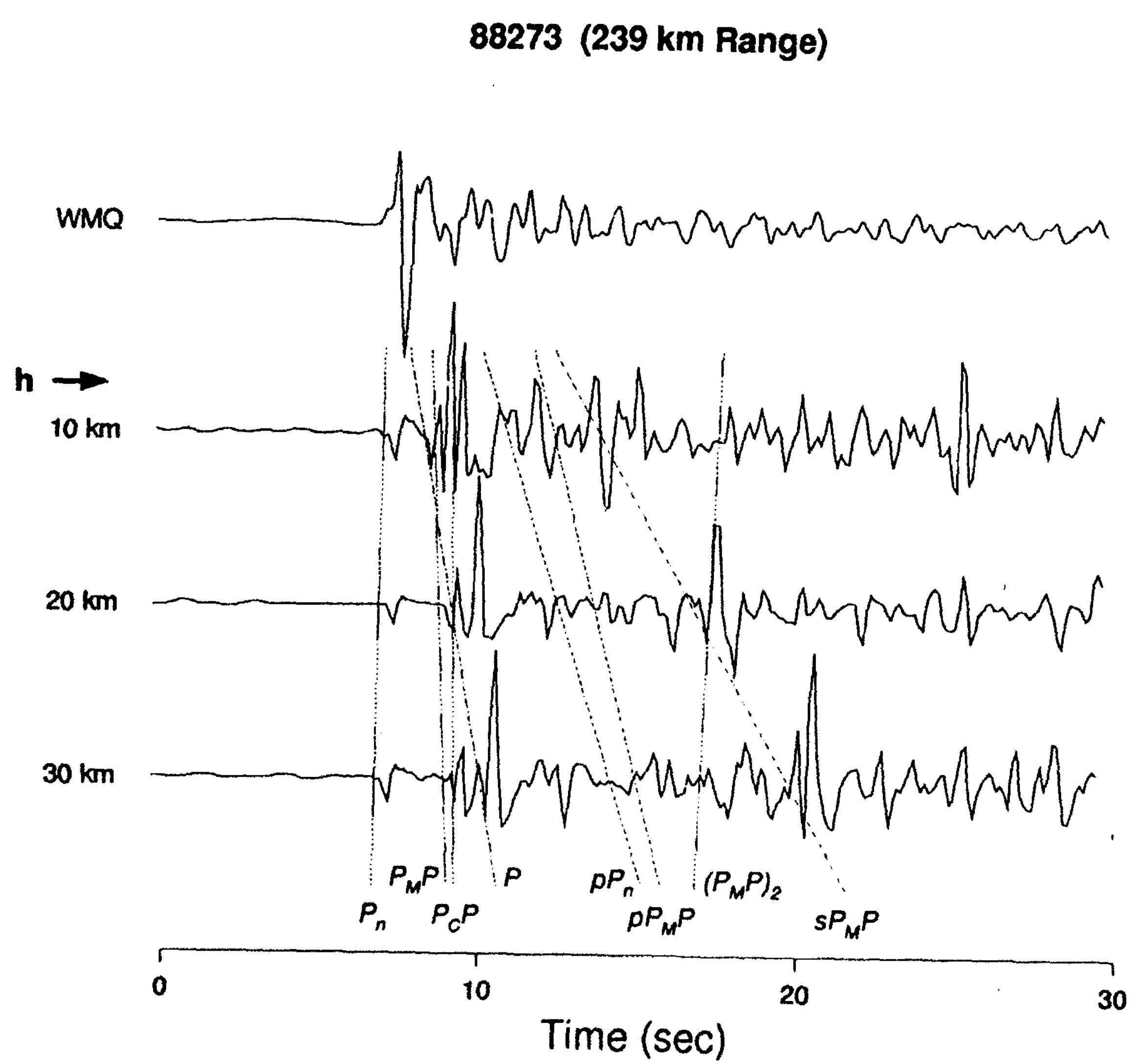

Fig. 21 - Comparison of the observed P_n-P_g waveform for event 88273 (top trace) with F-K synthetics computed for source depths of 10, 20 and 30 km. The format is the same as in Figure 6.

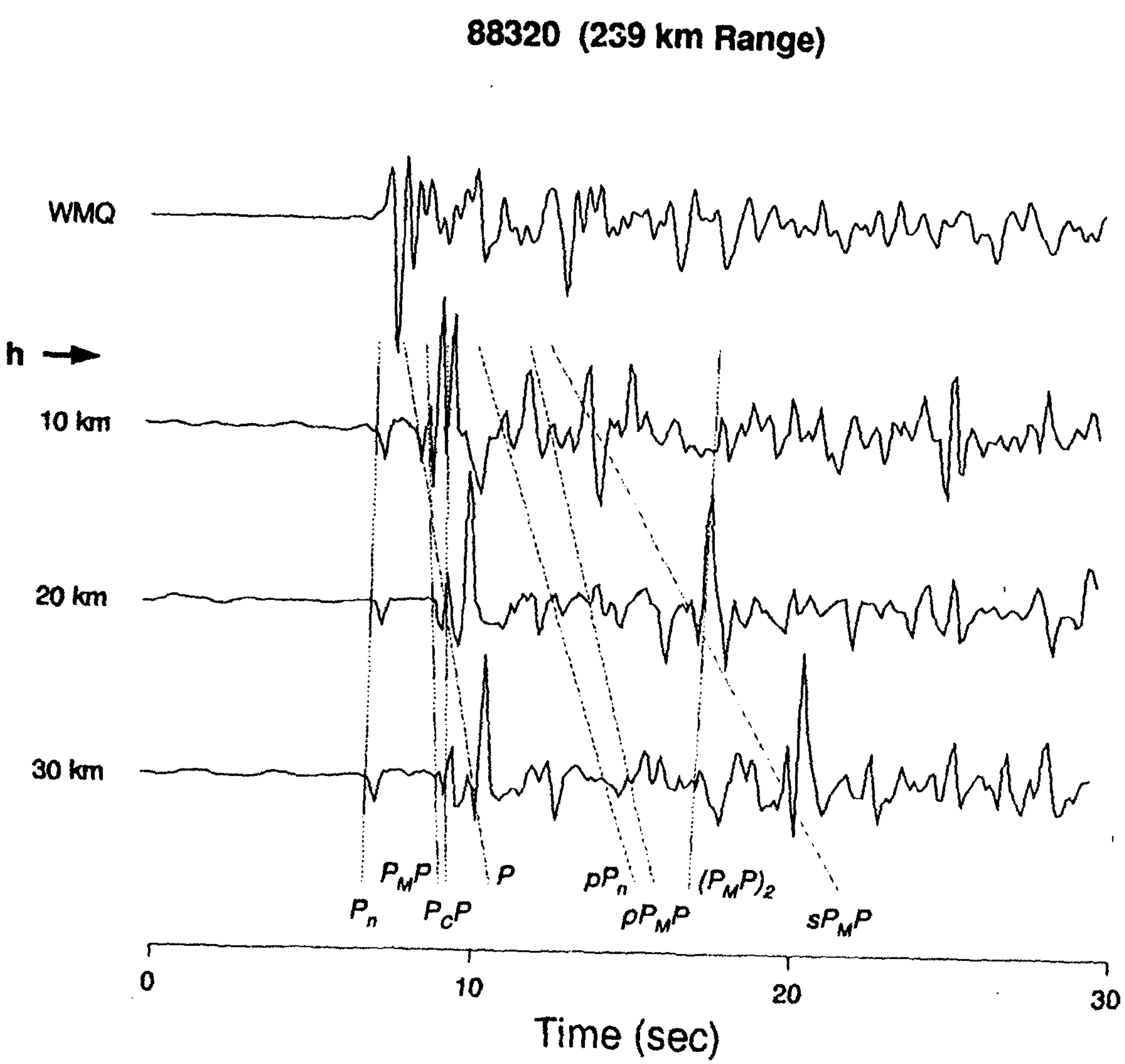

Fig. 22 - Comparison of the observed P_n-P_g waveform for event 88320 (top trace) with F-K synthetics computed for source depths of 10, 20 and 30 km. The format is the same as in Figure 6.

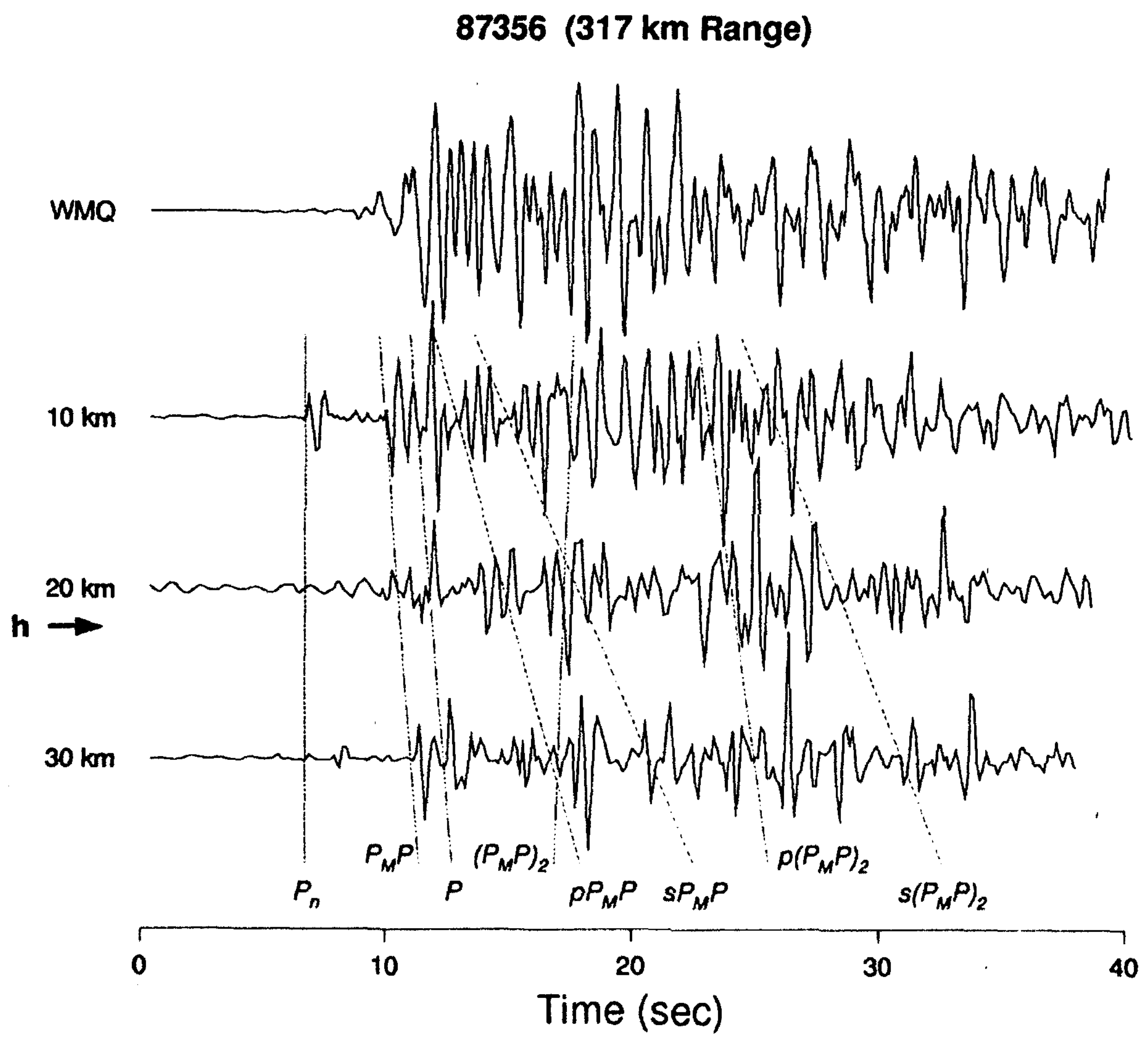

Fig. 23 - Comparison of the observed P_n-P_g waveform for event 87356 (top trace) with F-K synthetics computed for source depths of 10, 20 and 30 km. The format is the same as in Figure 6.

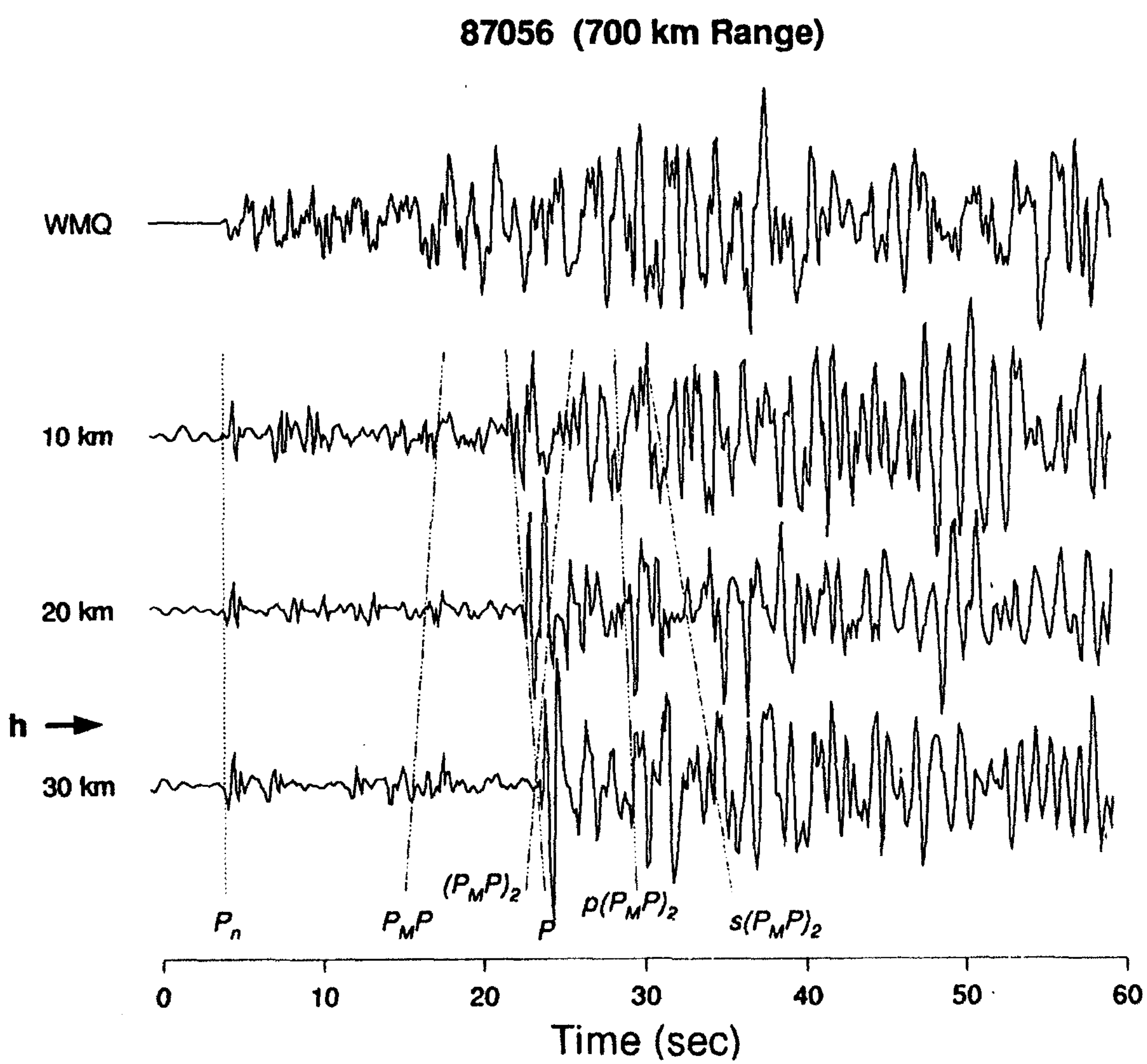

Fig. 24 - Comparison of the observed P_n-P_g waveform for event 87056 (top trace) with F-K synthetics computed for source depths of 10, 20 and 30 km. The format is the same as in Figure 6.

Prof. Thomas Ahrens
Seismological Lab, 252-21
Division of Geological & Planetary Sciences
California Institute of Technology
Pasadena, CA 91125

Prof. Keiiti Aki
Center for Earth Sciences
University of Southern California
University Park
Los Angeles, CA 90089-0741

Prof. Shelton Alexander
Geosciences Department
403 Deike Building
The Pennsylvania State University
University Park, PA 16802

Prof. Charles B. Archambeau
CIRES
University of Colorado
Boulder, CO 80309

Dr. Thomas C. Bache, Jr.
Science Applications Int'l Corp.
10260 Campus Point Drive
San Diego, CA 92121 (2 copies)

Prof. Muawia Barazangi
Institute for the Study of the Continent
Cornell University
Ithaca, NY 14853

Dr. Jeff Barker
Department of Geological Sciences
State University of New York
at Binghamton
Vestal, NY 13901

Dr. Douglas R. Baumgardt
ENSCO, Inc
5400 Port Royal Road
Springfield, VA 22151-2388

Dr. Susan Beck
Department of Geosciences
Building #77
University of Arizona
Tuscon, AZ 85721

Dr. T.J. Bennett
S-CUBED
A Division of Maxwell Laboratories
11800 Sunrise Valley Drive, Suite 1212
Reston, VA 22091

Dr. Robert Blandford
AFTAC/TT, Center for Seismic Studies
1300 North 17th Street
Suite 1450
Arlington, VA 22209-2308

Dr. Stephen Bratt
ARPA/NMRO
3701 North Fairfax Drive
Arlington, VA 22203-1714

Dr. Lawrence Burdick
IGPP, A-025
Scripps Institute of Oceanography
University of California, San Diego
La Jolla, CA 92093

Dr. Robert Burridge
Schlumberger-Doll Research Center
Old Quarry Road
Ridgefield, CT 06877

Dr. Jerry Carter
Center for Seismic Studies
1300 North 17th Street
Suite 1450
Arlington, VA 22209-2308

Dr. Eric Chael
Division 9241
Sandia Laboratory
Albuquerque, NM 87185

Dr. Martin Chapman
Department of Geological Sciences
Virginia Polytechnical Institute
21044 Derring Hall
Blacksburg, VA 24061

Prof. Vernon F. Cormier
Department of Geology & Geophysics
U-45, Room 207
University of Connecticut
Storrs, CT 06268

Prof. Steven Day
Department of Geological Sciences
San Diego State University
San Diego, CA 92182

Marvin Denny
U.S. Department of Energy
Office of Arms Control
Washington, DC 20585

Dr. Zoltan Der
ENSCO, Inc.
5400 Port Royal Road
Springfield, VA 22151-2388

Prof. Adam Dziewonski
Hoffman Laboratory, Harvard University
Dept. of Earth Atmos. & Planetary Sciences
20 Oxford Street
Cambridge, MA 02138

Prof. John Ebel
Department of Geology & Geophysics
Boston College
Chestnut Hill, MA 02167

Eric Fielding
SNEE Hall
INSTOC
Cornell University
Ithaca, NY 14853

Dr. Mark D. Fisk
Mission Research Corporation
735 State Street
P.O. Drawer 719
Santa Barbara, CA 93102

Prof Stanley Flatte
Applied Sciences Building
University of California, Santa Cruz
Santa Cruz, CA 95064

Dr. John Foley
NER-Geo Sciences
1100 Crown Colony Drive
Quincy, MA 02169

Prof. Donald Forsyth
Department of Geological Sciences
Brown University
Providence, RI 02912

Dr. Art Frankel
U.S. Geological Survey
922 National Center
Reston, VA 22092

Dr. Cliff Frolich
Institute of Geophysics
8701 North Mopac
Austin, TX 78759

Dr. Holly Given
IGPP, A-025
Scripps Institute of Oceanography
University of California, San Diego
La Jolla, CA 92093

Dr. Jeffrey W. Given
SAIC
10260 Campus Point Drive
San Diego, CA 92121

Dr. Dale Glover
Defense Intelligence Agency
ATTN: ODT-1B
Washington, DC 20301

Dan N. Hagedon
Pacific Northwest Laboratories
Battelle Boulevard
Richland, WA 99352

Dr. James Hannon
Lawrence Livermore National Laboratory
P.O. Box 808
L-205
Livermore, CA 94550

Prof. David G. Harkrider
Seismological Laboratory
Division of Geological & Planetary Sciences
California Institute of Technology
Pasadena, CA 91125

Prof. Danny Harvey
CIRES
University of Colorado
Boulder, CO 80309

Prof. Donald V. Helmberger
Seismological Laboratory
Division of Geological & Planetary Sciences
California Institute of Technology
Pasadena, CA 91125

Prof. Eugene Herrin
Institute for the Study of Earth and Man
Geophysical Laboratory
Southern Methodist University
Dallas, TX 75275

Prof. Robert B. Herrmann
Department of Earth & Atmospheric Sciences
St. Louis University
St. Louis, MO 63156

Prof. Lane R. Johnson
Seismographic Station
University of California
Berkeley, CA 94720

Prof. Thomas H. Jordan
Department of Earth, Atmospheric &
Planetary Sciences
Massachusetts Institute of Technology
Cambridge, MA 02139

Prof. Alan Kafka
Department of Geology & Geophysics
Boston College
Chestnut Hill, MA 02167

Robert C. Kemerait
ENSCO, Inc.
445 Pineda Court
Melbourne, FL 32940

Dr. Karl Koch
Institute for the Study of Earth and Man
Geophysical Laboratory
Southern Methodist University
Dallas, Tx 75275

Dr. Max Koontz
U.S. Dept. of Energy/DP 5
Forrestal Building
1000 Independence Avenue
Washington, DC 20585

Dr. Richard LaCoss
MIT Lincoln Laboratory, M-200B
P.O. Box 73
Lexington, MA 02173-0073

Dr. Fred K. Lamb
University of Illinois at Urbana-Champaign
Department of Physics
1110 West Green Street
Urbana, IL 61801

Prof. Charles A. Langston
Geosciences Department
403 Deike Building
The Pennsylvania State University
University Park, PA 16802

Jim Lawson, Chief Geophysicist
Oklahoma Geological Survey
Oklahoma Geophysical Observatory
P.O. Box 8
Leonard, OK 74043-0008

Prof. Thorne Lay
Institute of Tectonics
Earth Science Board
University of California, Santa Cruz
Santa Cruz, CA 95064

Dr. William Leith
U.S. Geological Survey
Mail Stop 928
Reston, VA 22092

Mr. James F. Lewkowicz
Phillips Laboratory/GPEH
29 Randolph Road
Hanscom AFB, MA 01731-3010(2 copies)

Mr. Alfred Lieberman
ACDA/VI-OA State Department Building
Room 5726
320-21st Street, NW
Washington, DC 20451

Prof. L. Timothy Long
School of Geophysical Sciences
Georgia Institute of Technology
Atlanta, GA 30332

Dr. Randolph Martin, III
New England Research, Inc.
76 Olcott Drive
White River Junction, VT 05001

Dr. Robert Masse
Denver Federal Building
Box 25046, Mail Stop 967
Denver, CO 80225

Dr. Gary McCartor
Department of Physics
Southern Methodist University
Dallas, TX 75275

Prof. Thomas V. McEvilly
Seismographic Station
University of California
Berkeley, CA 94720

Dr. Art McGarr
U.S. Geological Survey
Mail Stop 977
U.S. Geological Survey
Menlo Park, CA 94025

Dr. Keith L. McLaughlin
S-CUBED
A Division of Maxwell Laboratory
P.O. Box 1620
La Jolla, CA 92038-1620

Stephen Miller & Dr. Alexander Florence
SRI International
333 Ravenswood Avenue
Box AF 116
Menlo Park, CA 94025-3493

Prof. Bernard Minster
IGPP, A-025
Scripps Institute of Oceanography
University of California, San Diego
La Jolla, CA 92093

Prof. Brian J. Mitchell
Department of Earth & Atmospheric Sciences
St. Louis University
St. Louis, MO 63156

Mr. Jack Murphy
S-CUBED
A Division of Maxwell Laboratory
11800 Sunrise Valley Drive, Suite 1212
Reston, VA 22091 (2 Copies)

Dr Keith K. Nakanishi
Lawrence Livermore National Laboratory
L-025
P.O. Box 808
Livermore, CA 94550

Prof. John A. Orcutt
IGPP, A-025
Scripps Institute of Oceanography
University of California, San Diego
La Jolla, CA 92093

Prof. Jeffrey Park
Kline Geology Laboratory
P.O. Box 6666
New Haven, CT 06511-8130

Dr. Howard Patton
Lawrence Livermore National Laboratory
L-025
P.O. Box 808
Livermore, CA 94550

Dr. Frank Pilotte
HQ AFTAC/TT
130 South Highway A1A
Patrick AFB, FL 32925-3002

Dr. Jay J. Pulli
Radix Systems, Inc.
201 Perry Parkway
Gaithersburg, MD 20877

Dr. Robert Reinke
ATTN: FCTVTD
Field Command
Defense Nuclear Agency
Kirtland AFB, NM 87115

Prof. Paul G. Richards
Lamont-Doherty Geological Observatory
of Columbia University
Palisades, NY 10964

Mr. Wilmer Rivers
Teledyne Geotech
314 Montgomery Street
Alexandria, VA 22314

Dr. Alan S. Ryall, Jr.
ARPA/NMRO
3701 North Fairfax Drive
Arlington, VA 22209-1714

Dr. Richard Sailor
TASC, Inc.
55 Walkers Brook Drive
Reading, MA 01867

Prof. Charles G. Sammis
Center for Earth Sciences
University of Southern California
University Park
Los Angeles, CA 90089-0741

Prof. Christopher H. Scholz
Lamont-Doherty Geological Observatory
of Columbia University
Palisades, NY 10964

Dr. Susan Schwartz
Institute of Tectonics
1156 High Street
Santa Cruz, CA 95064

Secretary of the Air Force
(SAFRD)
Washington, DC 20330

Office of the Secretary of Defense
DDR&E
Washington, DC 20330

Thomas J. Sereno, Jr.
Science Application Int'l Corp.
10260 Campus Point Drive
San Diego, CA 92121

Dr. Michael Shore
Defense Nuclear Agency/SPSS
6801 Telegraph Road
Alexandria, VA 22310

Dr. Robert Shumway
University of California Davis
Division of Statistics
Davis, CA 95616

Dr. Matthew Sibol
Virginia Tech
Seismological Observatory
4044 Derring Hall
Blacksburg, VA 24061-0420

Prof. David G. Simpson
IRIS, Inc.
1616 North Fort Myer Drive
Suite 1050
Arlington, VA 22209

Donald L. Springer
Lawrence Livermore National Laboratory
L-025
P.O. Box 808
Livermore, CA 94550

Dr. Jeffrey Stevens
S-CUBED
A Division of Maxwell Laboratory
P.O. Box 1620
La Jolla, CA 92038-1620

Lt. Col. Jim Stobie
ATTN: AFOSR/NL
110 Duncan Avenue
Bolling AFB
Washington, DC 20332-0001

Prof. Brian Stump
Institute for the Study of Earth & Man
Geophysical Laboratory
Southern Methodist University
Dallas, TX 75275

Prof. Jeremiah Sullivan
University of Illinois at Urbana-Champaign
Department of Physics
1110 West Green Street
Urbana, IL 61801

Prof. L. Sykes
Lamont-Doherty Geological Observatory
of Columbia University
Palisades, NY 10964

Dr. David Taylor
ENSCO, Inc.
445 Pineda Court
Melbourne, FL 32940

Dr. Steven R. Taylor
Los Alamos National Laboratory
P.O. Box 1663
Mail Stop C335
Los Alamos, NM 87545

Prof. Clifford Thurber
University of Wisconsin-Madison
Department of Geology & Geophysics
1215 West Dayton Street
Madison, WS 53706

Prof. M. Nafi Toksoz
Earth Resources Lab
Massachusetts Institute of Technology
42 Carleton Street
Cambridge, MA 02142

Dr. Larry Turnbull
CIA-OSWR/NED
Washington, DC 20505

Dr. Gregory van der Vink
IRIS, Inc.
1616 North Fort Myer Drive
Suite 1050
Arlington, VA 22209

Dr. Karl Veith
EG&G
5211 Auth Road
Suite 240
Suitland, MD 20746

Prof. Terry C. Wallace
Department of Geosciences
Building #77
University of Arizona
Tuscon, AZ 85721

Dr. Thomas Weaver
Los Alamos National Laboratory
P.O. Box 1663
Mail Stop C335
Los Alamos, NM 87545

Dr. William Wortman
Mission Research Corporation
8560 Cinderbed Road
Suite 700
Newington, VA 22122

Prof. Francis T. Wu
Department of Geological Sciences
State University of New York
at Binghamton
Vestal, NY 13901

ARPA, OASB/Library
3701 North Fairfax Drive
Arlington, VA 22203-1714

HQ DNA
ATTN: Technical Library
Washington, DC 20305

Defense Intelligence Agency
Directorate for Scientific & Technical Intelligence
ATTN: DTIB
Washington, DC 20340-6158

Defense Technical Information Center
Cameron Station
Alexandria, VA 22314 (2 Copies)

TACTEC
Battelle Memorial Institute
505 King Avenue
Columbus, OH 43201 (Final Report)

Phillips Laboratory
ATTN: XPG
29 Randolph Road
Hanscom AFB, MA 01731-3010

Phillips Laboratory
ATTN: GPE
29 Randolph Road
Hanscom AFB, MA 01731-3010

Phillips Laboratory
ATTN: TSML
5 Wright Street
Hanscom AFB, MA 01731-3004

Phillips Laboratory
ATTN: PL/SUL
3550 Aberdeen Ave SE
Kirtland, NM 87117-5776 (2 copies)

Dr. Michel Bouchon
I.R.I.G.M.-B.P. 68
38402 St. Martin D'Heres
Cedex, FRANCE

Dr. Michel Campillo
Observatoire de Grenoble
I.R.I.G.M.-B.P. 53
38041 Grenoble, FRANCE

Dr. Kin Yip Chun
Geophysics Division
Physics Department
University of Toronto
Ontario, CANADA

Prof. Hans-Peter Harjes
Institute for Geophysic
Ruhr University/Bochum
P.O. Box 102148
4630 Bochum 1, GERMANY

Prof. Eystein Husebye
NTNF/NORSAR
P.O. Box 51
N-2007 Kjeller, NORWAY

David Jepsen
Acting Head, Nuclear Monitoring Section
Bureau of Mineral Resources
Geology and Geophysics
G.P.O. Box 378, Canberra, AUSTRALIA

Ms. Eva Johannisson
Senior Research Officer
FOA
S-172 90 Sundbyberg, SWEDEN

Dr. Peter Marshall
Procurement Executive
Ministry of Defense
Blacknest, Brimpton
Reading FG7-FRS, UNITED KINGDOM

Dr. Bernard Massinon, Dr. Pierre Mechler
Societe Radiomana
27 rue Claude Bernard
75005 Paris, FRANCE (2 Copies)

Dr. Svein Mykkeltveit
NTNT/NORSAR
P.O. Box 51
N-2007 Kjeller, NORWAY (3 Copies)

Prof. Keith Priestley
University of Cambridge
Bullard Labs, Dept. of Earth Sciences
Madingley Rise, Madingley Road
Cambridge CB3 OEZ, ENGLAND

Dr. Jorg Schlittenhardt
Federal Institute for Geosciences & Nat'l Res.
Postfach 510153
D-30631 Hannover, GERMANY

Dr. Johannes Schweitzer
Institute of Geophysics
Ruhr University/Bochum
P.O. Box 1102148
4360 Bochum 1, GERMANY

Trust & Verify
VERTIC
8 John Adam Street
London WC2N 6EZ, ENGLAND